LOW TEMPERATURE STEADY STATE NONLINEAR SPECTROSCOPY OF EXCITONS IN MONOLAYER $MoSe_2$

by

Muhed S. Rana

_____

A Dissertation Submitted to the Faculty of the

DEPARTMENT OF PHYSICS

In Partial Fulfillment of the Requirements

For the Degree of

DOCTOR OF PHILOSOPHY

In the Graduate College

THE UNIVERSITY OF ARIZONA

2021

THE UNIVERSITY OF ARIZONA
GRADUATE COLLEGE

As members of the Dissertation Committee, we certify that we have read the dissertation prepared by: Muhed S. Rana, titled: Low Temperature Steady State Nonlinear Spectroscopy of Excitons in Monolayer $MoSe_2$

and recommend that it be accepted as fulfilling the dissertation requirement for the Degree of Doctor of Philosophy.

John Schaibley — Date: Aug 18, 2021
John Schaibley

Brian LeRoy — Date: Aug 18, 2021
Brian LeRoy

R. Binder — Date: Aug 18, 2021
Rolf Binder

Weigang Wang — Date: Aug 18, 2021
Weigang Wang

Arvinder Sandhu — Date: Aug 18, 2021
Arvinder Sandhu

Final approval and acceptance of this dissertation is contingent upon the candidate's submission of the final copies of the dissertation to the Graduate College.

I hereby certify that I have read this dissertation prepared under my direction and recommend that it be accepted as fulfilling the dissertation requirement.

John Schaibley — Date: Aug 18, 2021
John Schaibley
Dissertation Committee Chair
Department of Physics

Acknowledgements

First and foremost, I would like to thank my advisor, John, who's been nothing but patient with me in spite of all of my failures, mistakes, and my family's struggles. He took me in as a stray third year theorist, personally having very little idea what I was looking for. His guidance is the entire reason I have gotten to the point where I am now. Even during COVID times, despite all the frustration from the labs at my internship being shut down, and the frustration of being on the other side of the country, he made every effort to ensure I was on track to graduation. The skills I learned in the lab, the process of building a lab from scratch, the work environment, various collaborations with other groups, and even my laundry list of failures in the lab have been rewarding.

The entire lab group – Christine Muccianti, Fateme Mahdikanysarveyjahany, Dan Shanks, Matt Klein, and Hongfei Zheng, Bekele Badada, Adam Alfrey, Max McKie, Jonathan Friduss, Miguel Briceno, Alex Ruthford and so many other undergrads – have all been so fun and so warm to the point that graduate school has been bearable. All of us would go out of our way to help each other, between revising theses and manuscripts, providing materials, doing processes for me which I am otherwise unable to do. I often joke that I never get a respite from my two sisters because I always have to come back to the lab with Fateme and Christine. I would also like to thank Brian LeRoy, who has been, in a sense, the second advisor to everyone in our lab. The LeRoy lab has been our second lab with Alex Brasington, Zhiming Zhang, Rachel Nieken, and Anna Roche essentially feeling like members of our lab. We call our whole little basement complex the "LeRaibley labs" and I'm going to miss the entire little system we had.

There are countless people to thank from the administration who have dealt with me for my entire 7 years here. Between Gardie ensuring everything about graduate school bureaucracy was smooth for us, to Shane always making sure we eventually get paid, to Carmen keeping track

of everything and keeping the department running and smooth. I can safely say that any issues I have had here have been resolved very swiftly and painlessly.

I'd like to thank Chris Stevens and Josh Hendrickson for accommodating me at the Wright-Patterson Air Force Base. There were a lot of very unfortunate circumstances, but they stood patient and supported me through the toughest times of my life.

To the Meyerhoff Scholarship Program, who paid for my entire undergrad and advised me through to my career goals. There's a countless number of people to thank from there, and I cannot list them all – between my summer bridge counselors, Mr. Toliver, the entire Meyerhoff Staff, and my cohort members – or else my thesis would be about them and not me. Being on the other side of the country has made things difficult and yet we've always made effort to be around each other when we're home. The random messages and calls have kept me pulling through some these tumultuous times.

And finally, my family. Firstly, my dad, Shamim Rana, who passed last year. He was the patriarch of the family, setting the roots for what we call the American branch of the Rana family. My mom, Riffat Rana, who is the strongest person on earth, taking care of us three crazy kids and tirelessly caring for my dad near the end. They brought us to America and the only thing on their mind, always, was to provide for us. We were not very fortunate for a long time when I was growing up but they made sure we had everything we needed. My sisters, Mahera and Arooj, my brother-in-law Kashaf, my niece Anya, and my countless cousins (blood related and not) have all been there through every step, constantly encouraging me through the worst of times. I truly don't think I would've made it through if not for all of them.

Dedication

For my dear, departed Abu.

Table of Contents

Figures and Tables

Abbreviations

hBN	Hexagonal Boron Nitride
TMD	Transition Metal Dichalcogenide
ML	Monolayer
TDSE	Time-dependent Schrodinger Equation
RWA	Rotating Wave Approximation
PL	Photoluminescence
SHG	Second Harmonic Generation
AFM	Atomic Force Microscope/Microscopy
PC	Polycarbonate
PDMS	Polydimethylsiloxane
EBL	Electron Beam Lithography
SEM	Scanning Electron Microscope/Microscopy
PMMA	Polymethyl Methacrylate
NPGS	Nano-Parameter Generation System
CW	Continuous Wave
AOM	Acousto-Optic Modulator
LIA	Lock-in Amplifier
DT/T	Differential Transmission divided by Transmission

e-h	electron-hole

Abstract

Transition metal dichalcogenides (TMDs), such as $MoSe_2$, can be thinned to a single layer molecular monolayer and combined with numerous atomically flat van der Waals materials to form novel heterostructures as a potential basis for quantum materials[1–3] and photoelectrodes for solar cells[4,5]. Monolayer TMDs exhibit tightly bounded excitons in both neutral and charged species, spin-valley physics, and strong non-linear properties when probed at the neutral and charged exciton (trion) resonances. Previous non-linear optical measurements have consisted of transient response from ultrafast pump lasers, however a systematic study of the steady state non-linear response is lacking.

In this thesis, I will discuss the fundamentals of two-dimensional van der Waals materials in Chapter 1. In Chapter 2, I discuss the fundamentals of non-linear optics as applied to 2-, 3-, and 4-level systems, as a method to model the non-linear optical response of $MoSe_2$. In Chapter 3, I discuss fabrication methods. In Chapter 4, I discuss our optical setups used to measure both linear and non-linear response of a TMD heterostructure.

In Chapter 5, I discuss the steady-state non-linear spectroscopy using a modulated two-color pump-probe system described in Chapter 4. We measure the non-linear response of hBN-encapsulated $MoSe_2$ We observe differential transmission (DT) signals associated with both the neutral exciton and the intrinsically doped trion response, showing a strong dependence on the intensity and polarization of the pump and probe beam. A non-linear signal was observed at the trion resonance that has not appeared in previous work. The results are first compared to a theoretical model based on a multi-level system, where the signal was compared to a biexciton resonance. We further explore these results by analyzing the results of a T-matrix formulation based on the exciton-exciton, exciton-trion, and trion-trion correlations. The parameters in the T-

matrix formalism can be tuned to reproduce the experimental DT results. The theory remains consistent with the assumption of exciton-trion correlations, the absence of a bound biexciton, and strong spin-mixing through incoherent spin-valley relaxation.

Chapter 1 - Properties of 2D Materials

Two dimensional (2D) materials are materials which consist of strong in-plane covalent/ionic bonds and a weak out-of-plane attractive van der Waals force, which allow bulk to be cleaved into thin layers easily[6,7]. The out-of-plane van der Waals force also allows for the formation of more complex heterostructures with many other thin materials[8,9]. In this chapter, I discuss the classifications of 2D materials as well as their various applications, notably graphene, hexagonal boron nitride (hBN), and $MoSe_2$.

1.1: Graphene and hBN

Graphene is a semimetal[10,11] consisting of carbon atoms arranged in a hexagonal lattice (Figure 1-1). Graphene lattices have inversion symmetry, and strong non-linear properties in the presence of electric fields[12–14]. Graphene has a 2.3% absorption rate per layer[15,16], and at monolayer possesses an approximately linear band structure[17,18] as shown in Figure 1-2b, which shows a zoom-in of the dispersion relation at the K point of the Brillouin zone. The zero-overlap at the of the valence and conduction band leads to high conductivity of graphene[19], allowing for electrons to exhibit photon-like linear dispersion in graphene[20,21], and allows for use as metal contacts in heterostructures[22,23].

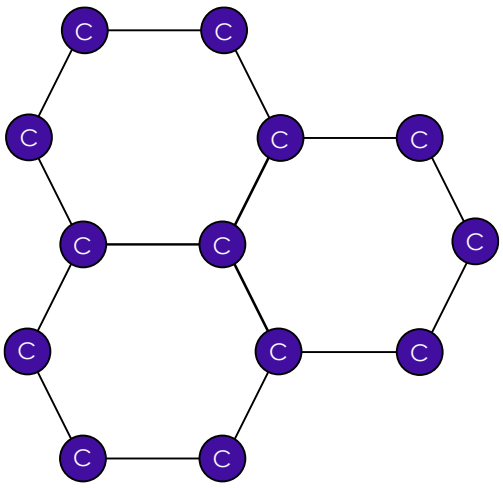

Figure 1-1. Atomic structure of graphene. hBN has a similar atomic structure with alternating B/N atoms.

hBN is a 2D material which is commonly used as an atomically flat substrate[24] allowing for easy pick-up of 2D materials and formation of high quality heterostructures[25]. It is an large gap semiconductor with a band gap of ~6 eV[26,27] which allows it to act as a dielectric tunneling barrier[28] in heterostructures. Its atomic structure is like graphene, however with alternating boron and nitrogen atoms instead of carbon atoms.

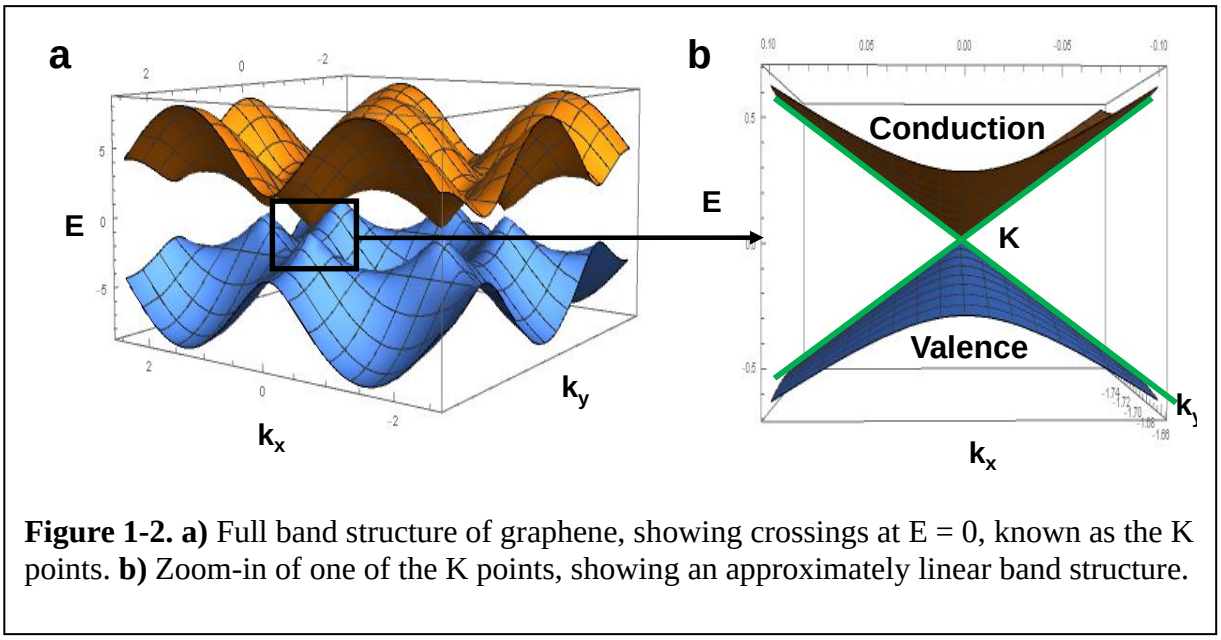

Figure 1-2. a) Full band structure of graphene, showing crossings at E = 0, known as the K points. **b)** Zoom-in of one of the K points, showing an approximately linear band structure.

1.2: Transition Metal Dichalcogenides

Another class of 2D materials is transition metal dichalcogenides (TMDs). The chemical formula of a TMD is MX_2 where M is a transition metal (such as Mo, W) and X is a chalcogen (such as S or Se). The focus of this thesis is on the very strong non-linear properties in heterostructures based around TMD semiconductors[29,30], notably $MoSe_2$. TMD semiconductors transition from an indirect band gap at bulk to a direct band gap when thinned to monolayer[5,31], which opens the door for optical applications utilizing monolayer TMD semiconductors. Figure 1-3 shows the atomic structure of a TMD, showing broken inversion symmetry.

1.3: Exciton Formation in $MoSe_2$

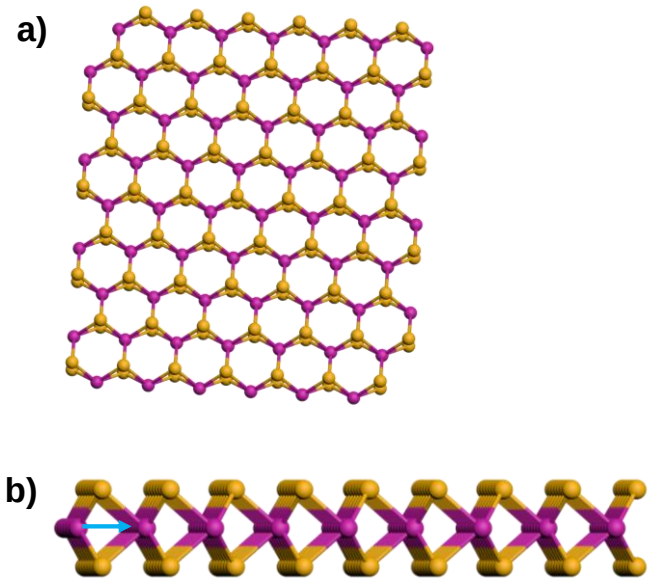

Figure 1-3. Atomic structure of a $MoSe_2$ lattice from **a)** the top-down and **b)** from the side. Like graphene, it has a hexagonal 2D lattice, however the transition metal bonds with four chalcogens and one chalcogen bonds with two transition metals apiece, creating a "double layer" at the selenium sites.

Figure 1-4 shows the formation of an electron-hole pair in a band diagram, where incident photons excite electrons from the valence band and into the conduction band. In doing so, the electron creates an excess positive charge (electron vacancy) in the valence band known as a hole. The excited charge carriers in the conduction band can recombine with the hole in the valence band and emit a photon with energy equal to the optical band gap. In $MoSe_2$, the exciton resonance has been experimentally shown to be ~1.65 eV. This recombination pair of an electron and hole is a quasiparticle known as an exciton. The optical response of $MoSe_2$ is dominated by the low energy "A" exciton with a binding energy of ~500 meV[32,33]. We should note that the energy of the exciton is below the electronic band gap due to the binding energy of the coulomb interaction from the electron-hole pair. The valence band of $MoSe_2$ contains a spin-orbit splitting of ~180 meV[34].

Excitons exist as both neutral (X^0) and charged ($X^{\pm}$) species which are referred to as trions. A neutral exciton is a simple electron/hole pair, whereas a trion is a bound three particle state composed of one electron and two holes (positive trion) or two electrons and one hole (negative trion). It is worth noting that trions have a lower emission energy than excitons due to their increased binding energy (~30 meV[32,33]) resulting from the extra carrier. It is also worth noting that many TMD semiconductors are intrinsically doped, leading to the natural formation of trions.

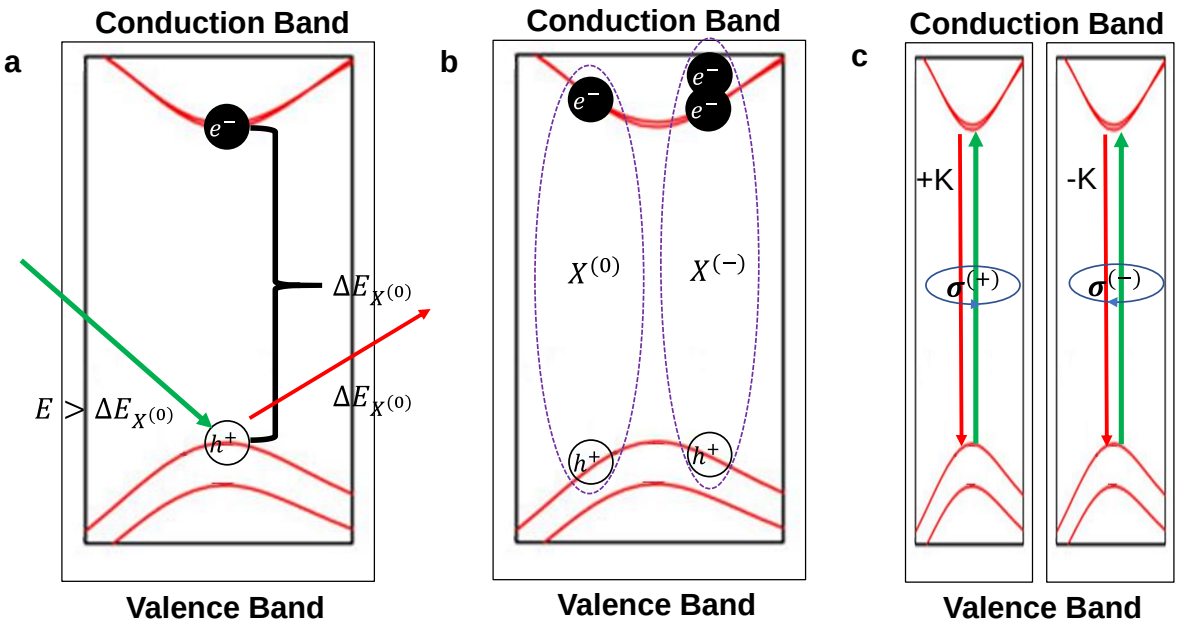

Figure 1-4. Exciton formation using a simple band structure model. **a)** Photoluminescence from an electron-hole pair, showing excitation and emission. **b)** Exciton and trion formation in the band structure, showing one electron/one hole for the exciton an two electrons/one hole for the trion. **c)** Valley optical selection rule in the +K valley. $MoSe_2$ has a valley pseudo-spin in the valence band, where each valley is coupled to a light of a particular helicity. In the upper +K (-K) valley, radiation is coupled to light of σ^+ (σ^-) helicity. [Zoom-in of band structure adapted from reference 33]

1.4: Valley Pseudo-Spin

The broken inversion symmetry of $MoSe_2$ allows for the contrasting physical properties of the K and -K valleys in the Brillouin zone. Figure 1-5 shows the valley properties of $MoSe_2$. The K and -K valleys of the Brillouin zone of $MoSe_2$ have equal energies and a resulting helicity-dependent optical selection rules[32,35,36]. In other words, the K and -K valleys are paired to light of σ^+ and σ^- polarization. This results in the creation of a valley pseudo-spin, which can potentially be used in various quantum information applications as a basis for a qubit state[37,38].

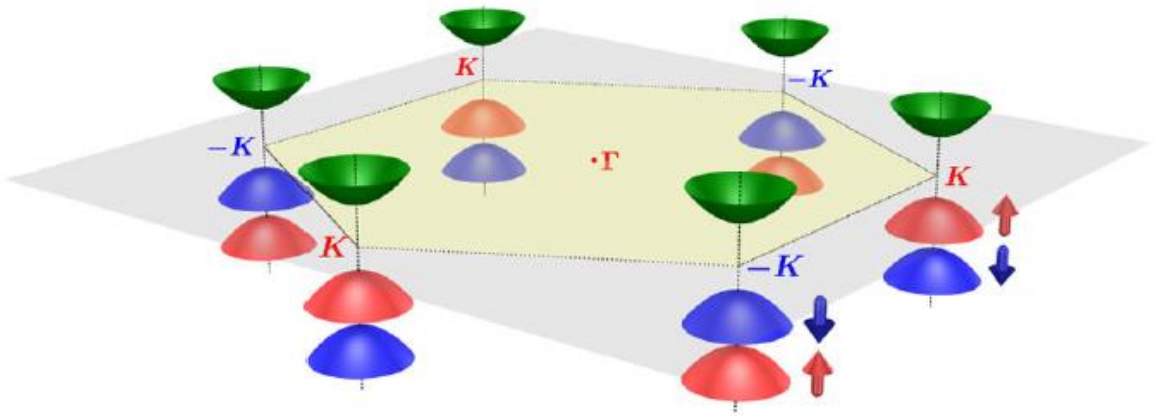

Figure 1-5. Schematic of the valley properties of a TMD semiconductor monolayer. The K and -K points both have helicity-dependent excitation as well as a ~180 meV spin-orbit splitting. [Figure adapted from reference 35]

1.5: TMD Heterostructures and Charging

The creation of TMD heterostructures using atomically flat hBN has led to the formation of high quality heterostructures and novel physics. For example, hBN can serve as a substrate for the $MoSe_2$, significantly reducing the effects of surface roughness and roughness from intermediate layers[39,40]. The encapsulation of $MoSe_2$ in hBN leads to longer exciton lifetimes, reduced exciton linewidth[41,42] and increased oxidation resistance[43,44]. hBN expands the scope of $MoSe_2$ by allowing

the creation of novel heterostructures which charge graphene contacts to finely control the doping level of $MoSe_2$ and control the formation of charged exciton species[28,45].

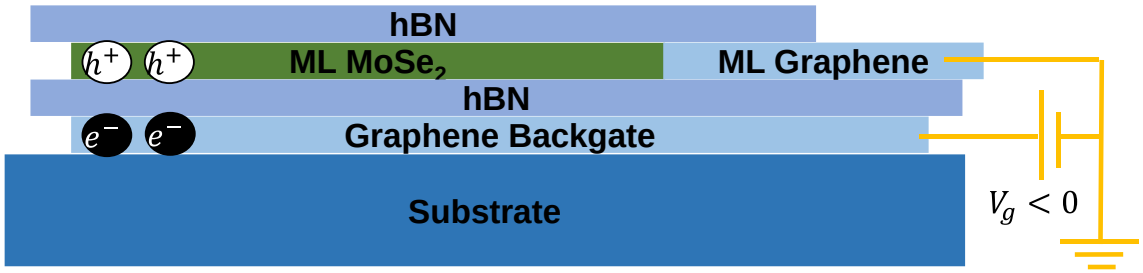

Figure 1-6. Example single-gated device with a graphene backgate, with a negative gate voltage. The voltage is applied to a gate which is electrically isolated from a graphene contact attached to the $MoSe_2$. The contact is connected to ground, which allows charges to tunnel through the hBN barrier. Because the gate voltage is negative, the $MoSe_2$ monolayer is hole-doped.

Figure 1-6 shows an example of a heterostructure composed of an hBN-encapsulated $MoSe_2$ monolayer, with a graphene gate on one side of the hBN-$MoSe_2$-hBN "sandwich" and a graphene contact directly attached to the $MoSe_2$. This device can be modeled as a capacitor with an hBN dielectric of constant κ = 2.89~3.03 (ML~Bulk)[46] on both sides of the TMD monolayer. The graphene gates are assigned a voltage to either electron-dope or hole-dope the $MoSe_2$ monolayer, depending on the polarity of the gate. The graphene contact to the device creates a ground.

Using a standard parallel place capacitor model, we know that

$$V_g = \frac{Q}{C} \quad (1.01)$$

and

$$C = \frac{k\,A\,\epsilon_0}{d} (1.02)$$

where *V, Q,* and *C* are respectively the voltage, capacitance, and charge on our "plates" (in this case, the TMD semiconductor and graphene gate). *A* is the surface area of the mutual area between the graphene gate and the TMD semiconductor, *d* is the thickness of the hBN separating them, and ϵ_0 is the free space permittivity. Combining equations 1.01 and 1.02, we obtain:

$$V_g = \frac{Q\,d}{k\,A\,\epsilon_0} (1.03)$$

We can re-arrange equation 1.03 and divide by the electron charge *e* to obtain the free carrier density of electrons *n*;

$$n = \frac{Q}{A\,e} = \frac{V_g\,k\,\epsilon_0}{d\,e} (1.04)$$

In doing this we can finely tune the doping level of the TMD in terms of the charge density (i.e., the number of charges per unit area).

Conclusion

2D Materials are a vast subcategory of material consisting of many varying types of materials with unique properties. These materials use a weak out-of-place van-der-Waals force to form heterostructures, which conventionally use materials such as graphene as a metal contact and hBN as insulating layers. TMD semiconductors are a category of materials which exhibit unique properties when thinned to monolayer. Combining graphene, hBN, and TMD semiconductors leads to novel devices utilizing electric fields to create novel heterostructures for optoelectronic applications.

Chapter 2 - Nonlinear Optics and Density Matrix Formalism

The linear and nonlinear optical response of excitons in monolayer transition metal dichalcogenide (TMD) semiconductors has been the subject of intense research over the past decade for their potential in various optoelectronic applications such as the creation of optical switches, buffers, and modulators which mediate interactions between two beams[47–49]. Previous two-color optical pump-probe measurements, to measure the third-order optical response of $MoSe_2$, have shown a redshift in the exciton signal, which have been attributed to band gap renormalization (BGR) effects[50]. A pump beam of varying energy E excites charge carriers from the valence band to the conduction band, which causes changes in the magnitude of an incident probe beam onto the sample. Carriers excited by the probe beam are then red-shifted due to various many-body interactions, e.g. increased binding energy resulting from Coulomb interaction from excess charge carriers resulting in a red-shift of the exciton energy.

Other nonlinear optical studies on $MoSe_2$ and similar TMD semiconductors have used ultrafast pump probe spectroscopy to probe the $MoSe_2$ exciton linewidth[51], trion formation dynamics[52,53], biexciton formation[53,54], and an Autler-Townes type exciton splitting[55]. The studies reveal that a strong resonant nonlinear response occurs when either pump or probe are resonant with neutral or charged exciton species. In this chapter we use the density matrix formalism of a multi-level system in the field-interaction representation to understand the nonlinear optical properties of an $MoSe_2$ exciton system, as well as a brief introduction into the T-matrix formalism we used to form a complete theory to describe the exciton dynamics in the system.

2.1: Fundamentals of Non-linear Optics

Light interaction leads to a macroscopic polarization density $\vec{P}$ in the medium, which can be described using the following equation:

$$\vec{P}(t) = \epsilon_0 \chi\left(\vec{E}(t)\right)\vec{E}(t) \quad (2.01)$$

Where ϵ_0 is the permittivity of free space, $\chi(\vec{E})$ is the susceptibility, and $\vec{E}(t)$ is the electric field. We can expand $\chi(\vec{E})$ using a power series and rewrite the susceptibility:

$$\chi(\vec{E}) = \chi^{(1)} + \chi^{(2)}\vec{E}(t) + \chi^{(3)}\vec{E}^2(t) + \cdots (2.02)$$

And plugging 2.02 back into 2.01…

$$\vec{P}(t) = \epsilon_0 \left(\chi^{(1)}\vec{E}(t) + \chi^{(2)}\vec{E}^2(t) + \chi^{(3)}\vec{E}^3(t) + \cdots\right)$$
$$= \vec{E}(t)\left(\vec{P}^{(1)}(t) + \vec{P}^{(2)}(t) + \vec{P}^{(3)}(t) + \cdots\right) \quad (2.03)$$

Where $\chi^{(n)}$ is the nth order susceptibility coefficient. Note that we will exclusively focus on the third order susceptibility in this thesis.

Nonlinear spectroscopy allows us to probe the fine structure of materials by probing the susceptibility of the material using two or more sources of excitation. Standard nonlinear optical techniques measure optical response as a function of varying parameters, such as optical frequency and delay time between pulses. Before we can calculate the non-linear optical effects, we must first develop our multi-level model.

2.2: Single-Atom Two-Level System in Field Interaction Representation

The field-interaction representation proves advantageous for us as it allows us to model the field-interaction between the $MoSe_2$ and any external light sources as a multi-level system with a perturbation effect resulting from the light source. The model is ultimately used to express the transitions and the optical response of a multi-level system as a function of elements of the density matrix ρ.

Suppose we write the Hamiltonian for a time-dependent Schrodinger equation (TDSE) of any single-atom-field interaction as the following;

$$\widehat{H}(\boldsymbol{r},t) = \widehat{H}_0(\boldsymbol{r}) + \hat{V}(\boldsymbol{r},t) \ (2.04)$$

Where $\widehat{H}_0(\boldsymbol{r})$ represents the time-independent Hamiltonian term and $\hat{V}(\boldsymbol{r},t)$ refers to the interaction of a classical, time-dependent field with the atom. The energy levels of any quantum system can be represented using equation 2.05;

$$\widehat{H}_0(\boldsymbol{r})\psi_n(\boldsymbol{r}) = E_n\psi_n(\boldsymbol{r}) \ (2.05)$$

Where $\psi_n(\boldsymbol{r})$ refers to the nth eigenstate of the quantum system. By using equation 2.05 in the TDSE, we can express the atom-field interaction using equation 2.06;

$$i\hbar\frac{\partial\psi(\boldsymbol{r},t)}{\partial t} = [\widehat{H}_0(\boldsymbol{r}) + \hat{V}(\boldsymbol{r},t)]\psi(\boldsymbol{r},t) \ (2.06)$$

The state vector ψ and equation 2.07 can be written as a sum of eigenstates;

$$\psi(\boldsymbol{r},t) = \sum_n a_n(t)\,\psi_n(\boldsymbol{r}) \ (2.07a)$$

$$i\hbar \sum_n \dot{a}_n(t)\, \psi_n(\boldsymbol{r}) = \widehat{H}_0(\boldsymbol{r}) \sum_n a_n(t)\, \psi_n(\boldsymbol{r}) + \hat{V}(\boldsymbol{r},t) \sum_n a_n(t)\, \psi_n(\boldsymbol{r}) \; (2.07b)$$

$$|\, \psi_n(\boldsymbol{r},t) > = \sum_n a_n(t)\, |\, n > \; (2.07c)$$

Where 2.07b is the amplitude representation and 2.07c is the Dirac notation representation of this state, and $a_n(t)$ refers to the time-dependent solution to the TDSE. By using the orthogonality of eigenstates, we can multiply equation 2.07b by $\psi_m(\boldsymbol{r})$ and integrate over $\boldsymbol{r}$ to find the time evolution of state amplitude $a_n(t)$;

$$i\hbar\, \dot{a}_n(t) = E_n a_n(t) + \sum_m V_{nm}(t)\, a_m(t) \; (2.08a)$$

$$i\hbar\, \dot{a}(t) = Ea(t) + V(t)a(t) \; (2.08b)$$

Where 2.08a is the amplitude representation of the interaction and 2.08b is a matrix equation. We can re-express the solutions to this equation using the interaction representation, which requires state amplitudes be constant without interaction. We start by expressing our eigenstate using equation 2.09;

$$\psi(\boldsymbol{r},t) = \sum_n c_n(t) e^{-i\frac{E_n t}{\hbar}}\, \psi_n(\boldsymbol{r}) \; (2.09a)$$

$$|\psi(t) > = \sum_n c_n(t) e^{-i\frac{E_n t}{\hbar}} |\, \psi_n > \; (2.09b)$$

Plugging 2.09a into 2.08b;

$$i\hbar\, \dot{c}_n(t) = \sum_m V_{nm}(t)\, c_m(t) e^{-i\omega_{nm} t} \; (2.10a)$$

$$\omega_{nm} = \frac{E_n - E_m}{\hbar} \ (2.10b)$$

Where we use ω_{nm} to refer to a transition frequency between two states n and m. Combining equation 2.09a and 2.07b, allows us to express $a_n(t)$ as a function of $c_n(t)$;

$$a_n(t) = c_n(t)e^{-i\frac{E_n t}{\hbar}} \ (2.11)$$

2.3: Application of Amplitude Representation to a Two-Level System

We can apply these equations to a two-level system interacting with an external electric field. We start by using an example external field defined by equation 2.12 and its corresponding interaction potential (2.13) obtained from the dipole approximation;

$$\boldsymbol{E}(t) = \hat{\boldsymbol{z}}|E_0(t)|\ cos[\omega t - \varphi(t)] \ (2.12)$$

$$\hat{V}(\boldsymbol{r}, t) \approx -\hat{\boldsymbol{\mu}} \cdot \boldsymbol{E}(\boldsymbol{R}, t) = e\hat{\boldsymbol{r}} \cdot \boldsymbol{E}(\boldsymbol{R}, t) \ (2.13)$$

Where $\hat{\boldsymbol{\mu}}$ refers to the atomic dipole moment operator. First we can define the ground state energy of a two level system as $-\hbar\omega_0/2$ and the excited state energy as $+\hbar\omega_0/2$, we can write our state amplitude $\boldsymbol{a}$ using a vector 2.14;

$$\boldsymbol{a} = \begin{pmatrix} a_1 \\ a_2 \end{pmatrix} (2.14)$$

And our corresponding interaction matrix V;

$$V = \begin{pmatrix} 0 & e\ z_{12}\ |E_0(t)|\ cos[\omega t - \varphi(t)] \\ e\ z_{21}|E_0(t)|\ cos[\omega t - \varphi(t)] & 0 \end{pmatrix} (2.15)$$

where we define our exciton dipole moment as $e\ z_{21} = e\ z_{12} = (\mu_z)_{21}$. This allows us to rewrite our Hamiltonian as;

$$H(t) = H_0 + V(t)$$

$$= \frac{1}{2}\begin{pmatrix} -\hbar\omega_0 & 2(\mu_z)_{21}\,|E_0(t)|\,cos[\omega t - \varphi(t)] \\ 2(\mu_z)_{21}\,|E_0(t)|\,cos[\omega t - \varphi(t)] & \hbar\omega_0 \end{pmatrix} \quad (2.16)$$

We can rewrite 2.16 in terms of the Rabi frequency Ω_0 to represent the strength of the interaction between the atom and the external radiation, then use equation 2.16 to calculate the values of the interaction terms in amplitude representation (2.17b);

$$\Omega_0(t) = \frac{2(\mu_z)_{21}\,|E_0(t)|}{\hbar} \quad (2.17a)$$

$$i\hbar\,\dot{a}_n(t) = \frac{\hbar}{2}\begin{pmatrix} -\omega_0 & \Omega_0(t)\cos[\omega t - \varphi(t)] \\ \Omega_0(t)\cos[\omega t - \varphi(t)] & \omega_0 \end{pmatrix} a(t) \quad (2.17b)$$

We can simplify this equation to adhere to our experimental conditions by assuming that the amplitude and phase of the field are slowly varying in comparison to the pump energy (ω). If ω is close to ω_0 ($\frac{(\omega_0-\omega)}{(\omega_0+\omega)} \ll 1$) then we can rewrite equation 2.17b as;

$$i\hbar\,\dot{a}_n(t) = \frac{\hbar}{2}\begin{pmatrix} -\omega_0 & \Omega_0(t)e^{-i\omega t} + \Omega_0^*(t)e^{i\omega t} \\ \Omega_0(t)e^{-i\omega t} + \Omega_0^*(t)e^{i\omega t} & \omega_0 \end{pmatrix} a(t) \quad (2.18)$$

In the interaction representation, using equation 2.08, we can rewrite this as;

$$i\hbar\,\dot{c}_n(t) = \frac{\hbar}{2}\begin{pmatrix} 0 & \Omega_0(t)e^{-i(\omega+\omega_0)t} + \Omega_0^*(t)e^{-i\delta t} \\ \Omega_0(t)e^{-i\delta t} + \Omega_0^*(t)e^{i(\omega+\omega_0)t} & 0 \end{pmatrix} c(t) \quad (2.19)$$

Where $\delta = \omega_0 - \omega$. For a sufficiently small value of δ, the off-diagonal terms can be separated into a slow and fast oscillating term. For $\frac{\delta}{(\omega_0+\omega)} \ll 1$, we can use the rotating wave approximation – also known as the resonance approximation – to rewrite the field amplitudes as;

$$i\hbar\,\dot{a}_n(t) = \frac{\hbar}{2}\begin{pmatrix} -\omega_0 & \Omega_0^*(t)e^{i\omega t} \\ \Omega_0(t)e^{-i\omega t} & \omega_0 \end{pmatrix} a(t) \quad (2.20a)$$

$$i\hbar\,\dot{c}_n(t) = \frac{\hbar}{2}\begin{pmatrix} 0 & \Omega_0^*(t)e^{-i\delta t} \\ \Omega_0(t)e^{-i\delta t} & 0 \end{pmatrix} c(t) \quad (2.20b)$$

Where 2.20a is the amplitude representation and 2.20b is the interaction representation. We can then numerically solve for the atom-field interaction amplitudes for a two level system using either representation of equation 2.20.

2.4: Density Matrix Formalism

For a two level system, we can define our density matrix ρ;

$$\rho = \begin{pmatrix} \rho_{11} & \rho_{12} \\ \rho_{21} & \rho_{22} \end{pmatrix} \quad (2.21)$$

We can then express the time evolution of the density matrix using equation 2.22;

$$i\hbar\frac{\partial\rho}{\partial t} = [H, \rho] \quad (2.22)$$

By plugging equations 2.20a and 2.21 into equation 2.22, we can form series of equations to represent the two-level atom interacting with an external electric field;

$$i\hbar\begin{pmatrix}\dot{\rho}_{11} & \dot{\rho}_{12}\\ \dot{\rho}_{21} & \dot{\rho}_{22}\end{pmatrix} = \frac{\hbar}{2}\left[\begin{pmatrix}-\omega_0 & \Omega_0^*(t)e^{i\omega t}\\ \Omega_0(t)e^{-i\omega t} & \omega_0\end{pmatrix}\begin{pmatrix}\rho_{11} & \rho_{12}\\ \rho_{21} & \rho_{22}\end{pmatrix}\right.$$
$$\left. - \begin{pmatrix}\rho_{11} & \rho_{12}\\ \rho_{21} & \rho_{22}\end{pmatrix}\begin{pmatrix}-\omega_0 & \Omega_0^*(t)e^{i\omega t}\\ \Omega_0(t)e^{-i\omega t} & \omega_0\end{pmatrix}\right] (2.23)$$

We can also add terms to add spontaneous emission and collision terms and expand the matrix in equation 2.23 to create the following equations in the amplitude representation;

$$\dot{\rho}_{11}(t) = -i\,\chi^*(t)e^{i\omega t}\rho_{21}(t) + i\,\chi(t)e^{-i\omega t}\rho_{12}(t) + \gamma_2\rho_{22}(t)\ (2.24a)$$

$$\dot{\rho}_{22}(t) = i\,\chi^*(t)e^{i\omega t}\rho_{21}(t) - i\,\chi(t)e^{-i\omega t}\rho_{12}(t) - \gamma_2\rho_{22}(t)\ (2.24b)$$

$$\dot{\rho}_{12}(t) = i\omega_0\rho_{12}(t) - i\,\chi^*(t)e^{i\omega t}[\rho_{22}(t) - \rho_{11}(t)] - \gamma\rho_{12}(t)\ (2.24c)$$

$$\dot{\rho}_{21}(t) = -i\omega_0\rho_{21}(t) + i\,\chi^*(t)e^{-i\omega t}[\rho_{22}(t) - \rho_{11}(t)] - \gamma\rho_{21}(t)\ (2.24d)$$

$$\rho_{11} + \rho_{22} = 1\ (2.24e)$$

Where $\chi(t) = 2\Omega_0(t)$ and 2.24e is a statement of conservation of population. γ and γ_2 refer to decay constants which are proportional to the linewidth of the respective exciton and trion states. We can re-express these terms in the field-interaction representation to represent the two-level system and the interaction using the following equations in the RWA;

$$\tilde{\rho}_{11} = \rho_{11},$$

$$\tilde{\rho}_{12} = e^{-i\omega t}\rho_{12}$$

$$\tilde{\rho}_{21} = e^{i\omega t}\rho_{21}\ (2.25)$$

Therefore we can rewrite our series of equations for a two-level atom interacting with a nearly-resonant field as;

$$\dot{\rho}_{11}(t) = -i\,\chi^*(t)\tilde{\rho}_{21}(t) + i\,\chi(t)\tilde{\rho}_{12}(t) + \gamma_2\rho_{22}(t) \quad (2.26a)$$

$$\dot{\rho}_{22}(t) = i\,\chi^*(t)\tilde{\rho}_{21}(t) - i\,\chi(t)\tilde{\rho}_{12}(t) - \gamma_2\rho_{22}(t) \quad (2.26b)$$

$$\dot{\tilde{\rho}}_{12}(t) = i\delta\tilde{\rho}_{12}(t) - i\,\chi^*(t)[\rho_{22}(t) - \rho_{11}(t)] - \gamma\tilde{\rho}_{12}(t) \quad (2.26c)$$

$$\dot{\tilde{\rho}}_{21}(t) = -i\delta\tilde{\rho}_{21}(t) + i\,\chi^*(t)[\rho_{22}(t) - \rho_{11}(t)] - \gamma\tilde{\rho}_{21}(t) \quad (2.26d)$$

$$\rho_{11} + \rho_{22} = 1 \quad (2.26e)$$

Which we then use to solve for each individual element of ρ. The diagonal elements correspond to the evolution of each individual state whereas the off-diagonal elements refer to the transitions between the states in the near-resonant field.

2.5: Three- and Four-Level Cascade System in Field Interaction Representation

A three-level system can be modeled in three different ways; a cascade, V, and lambda system. The standard system consists of a three-level atom interacting with two external electric field sources, thereby factoring in nonlinear effects into three level calculations. Our calculations will be performed in the field-interaction representation to model a three level system near resonance. Note that our considerations are solely to the cascade system shown in Fig. 2.1.

In a cascade system, we can write a state vector using the following;

$$|\psi(t)> = \dot{c}_1(t)e^{i\omega t}|1> + \dot{c}_2(t)|2> + \dot{c}_3(t)e^{-i\omega' t}|3> \quad (2.27)$$

Where ω and ω' refer to the frequency of both external electric fields in contact with the system. We can use these energies to refer to the energies of a pump and a probe beam respectively in 2D

non-linear spectroscopy. Using similar arguments to Chapter 2.2, we can form a Hamiltonian similar to 2.19 in the field-interaction representation;

$$\tilde{H} = \begin{pmatrix} -\delta & \chi^* & 0 \\ \chi & 0 & \chi'^* \\ 0 & \chi' & \delta' \end{pmatrix} \quad (2.28)$$

By using a 3x3 density matrix combined with the Hamiltonian in equation 2.26, the time evolution from equation 2.22, and relaxation terms, we can construct a series of equations like equation 2.26. We can solve this series of equation in steady state, we can set all time-derivative terms to zero to solve for all values of ρ. We can use similar arguments and considerations to obtain the solution for the density matrix elements of a degenerate four level system (Figure 2-2), with the following corresponding Hamiltonian.

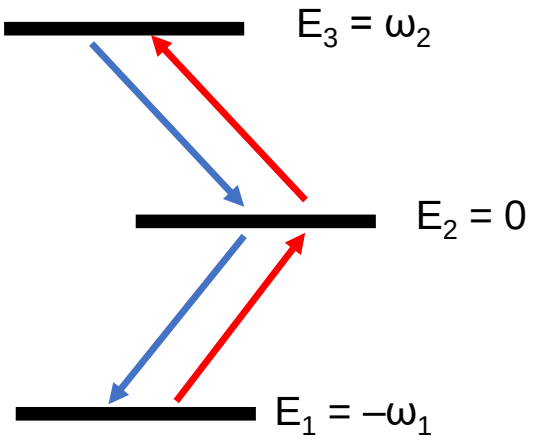

Figure 2-1. Three Level cascade diagram. Diagram of the model we use to construct our three-level system. In this model, charge carriers can be excited from State 1 to State 2, or State 2 to State 3, but not State 1 to State 3. In this model, we will refer to the Biexciton (XX) state as having energy ω_2, the Exciton ($X^{(0)}$) state as a zero-energy state, and the ground state as having energy $-\omega_1$.

$$\tilde{H} = \begin{pmatrix} -\omega_1 & \chi_{21} & \chi_{31} & 0 \\ \chi_{12} & -\omega & 0 & \chi_{42} \\ \chi_{13} & 0 & \omega' & \chi_{43} \\ 0 & \chi_{24} & \chi_{34} & -\omega_2 - \omega - \omega' \end{pmatrix} \quad (2.29)$$

Note that $\chi_{21} = \chi_{12}^{*}$ (and likewise for the other 3 pairs of rabi frequencies). The optical response of a particular transition is directly proportional to the corresponding density matrix element, allowing us to utilize our model to compare results from non-linear response techniques in chapter 4.

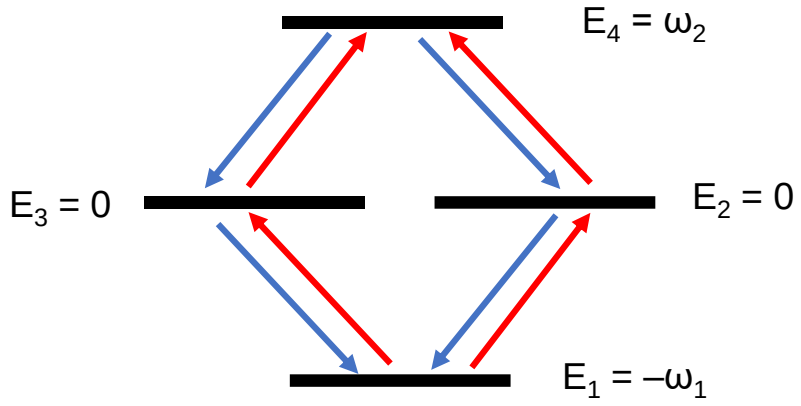

Figure 2-2. Diagram of the model we use to construct our four-level system. The only difference between this model and the model in Figure 2-1 is that this model accounts for the degenerate energy states that exist within TMDs; by doing this we factor in both the K and K' valleys within a TMD system. This also forbids any transition between state 3 and state 2. Like in Figure 2-1, the transition between State 1 and State 4 is also forbidden.

2.6: Lineshapes

Analyzing the steady-state non-linear DT/T lineshapes allows us to observe the processes which govern the interactions between different states. A standard Lorentzian lineshape uses the following equation:

$$L(E) = \frac{.5\,\Gamma}{(E - E_0)^2 + (.5\,\Gamma)^2} \quad (2.30)$$

Where Γ is the exciton linewidth and E_0 is the center of the emission.

A quick example of a redshift occurring because of a two-laser experiment is shown in Figure 2-3, where a small redshift in the transmission curve of Figure 2-3a results in the DT/T lineshape of Figure 2-3b. We can also extend this concept to view lineshapes which vary in the other parameters in equation 2.30. We can produce lineshapes using our density matrix formalism and replicate a differential signal, which we show in Chapter 5.

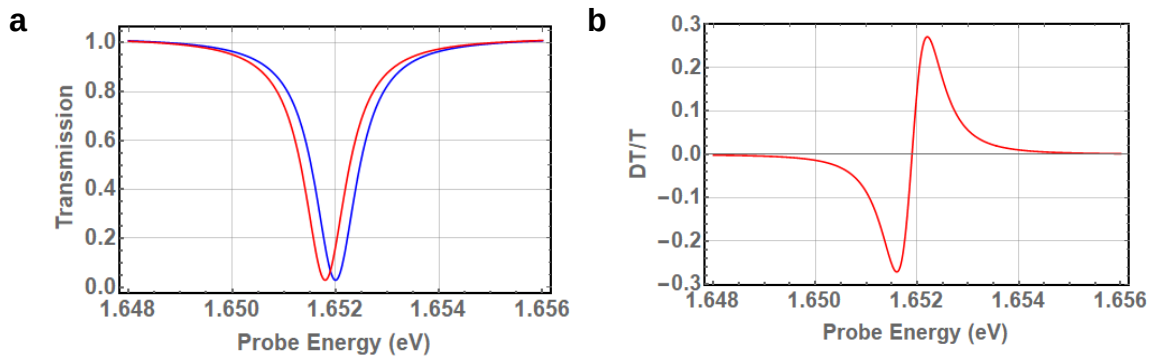

Figure 2-3. Sample formation of a DT/T lineshape. **a)** Calculated sample transmission spectrum. The blue line shows the probe transmission without the pump beam on. The red shows a red-shifted signal caused by the pump laser. **b)** The difference between the curves in a) divided by the blue curve. The signal shows a "minus-plus" lineshape.

2.7: T-Matrix Formalism

Although the Density Matrix formalism is a powerful tool, it is only as strong as the level model used to produce it. The level model will not generally be able to account for some of the specific interactions that result from the features, such as the coulomb interaction between a bound exciton and bound trion. The T-Matrix formalism is a scattering formalism used for computations of non-spherical particle scattering.[56] In this case, we can use this formalism to describe our system in terms of scattering of the three major particle interactions which govern the non-linear response – exciton-exciton, exciton-trion, and trion-trion[57]. Previous studies have shown a T-matrix

application to a GaAs semiconductor quantum well[58,59] to good accuracy, however the key difference in application of this theory is that there exists a trion state in TMD semiconductors.

The Lippman-Schwinger Equation can be defined in the following way:

$$|\Psi_k> = |\varphi_k> + \frac{1}{E - H_0 + i\gamma} V|\Psi_k> = |\varphi_k> + G_0\, V|\Psi_k> \quad (2.31)$$

Where $|\Psi>$ is the center of mass two-body wavefunction for the two-particle state, $|\varphi>$ are the eigenstates of the free-space non-interacting Hamiltonian H_0 with eigenvalues E, and V is the interaction potential between two particles, and G_0 is the Green operator. γ is a decay constant which ends up related to the linewidth of the interaction signal.

If we define the T-matrix as a transition matrix between the one-body and two-body state, we can say that

$$V|\Psi_k> = T|\varphi_k> \quad (2.32)$$

We can now multiply both sides of equation 2.31 by V, then rewrite in terms of equation 2.32,

$$T\,|\varphi_k> = V\,|\varphi_k> + VG_0\,T|\varphi_k> \quad (2.33)$$

Therefore, we can rewrite the Lippman-Schwinger equation solely in terms of operators:

$$T = V + V\,G_0\,T \quad (2.34)$$

We can now rewrite this equation in momentum space. In the notation of Kwong et al:

$$T(\boldsymbol{k},\boldsymbol{k}',\omega) = V(\boldsymbol{k},\boldsymbol{k}') + \sum_{q} V(\boldsymbol{k},\boldsymbol{q})G_0(\boldsymbol{q},\omega)T(\boldsymbol{q},\boldsymbol{k}',\omega) \quad (2.35)$$

Where $\boldsymbol{k}$ and $\boldsymbol{k}'$ are the final and initial relative momenta (respectively) of the scattered particles, $E = \hbar\omega$ refers to the total energy of the particles, and the Green's function serves as an interaction-free two-particle propagator. We can generalize the interaction potential using a generic square-integrable function $u(\boldsymbol{k})$;

$$V(\boldsymbol{k},\boldsymbol{k}') = \lambda\, u(\boldsymbol{k})u(\boldsymbol{k}') \quad (2.36)$$

Where λ represents the sign of the interaction; it is positive for a repulsive interaction and negative for an attractive interaction. We can combine 2.35 and 2.36 and factor:

$$T(\boldsymbol{k},\boldsymbol{k}',\omega) = \lambda\, u(\boldsymbol{k})\left(u(\boldsymbol{k}') + \sum_{q} u(\boldsymbol{q})\, G_0(\boldsymbol{q},\omega)T(\boldsymbol{q},\boldsymbol{k}',\omega)\right)$$

$$= \lambda\, u(\boldsymbol{k})(u(\boldsymbol{k}') + F(\boldsymbol{k}',\omega)) \quad (2.37)$$

Where we redefine the terms in the summation as a function $F(\boldsymbol{k}',\omega)$. If we multiply both sides of equation 2.37 by $u(\boldsymbol{k})G_0(\boldsymbol{k},\omega)$,

$$u(\boldsymbol{k})G_0(\boldsymbol{k},\omega)\, T(\boldsymbol{k},\boldsymbol{k}',\omega) = \lambda\, u^2(\boldsymbol{k})\, G_0(\boldsymbol{k},\omega)(u(\boldsymbol{k}') + F(\boldsymbol{k}',\omega)) \quad (2.38)$$

If we sum both sides up over $\boldsymbol{k}$, we can easily see the LHS becomes $F(\boldsymbol{k}',\omega)$ from equation 2.37, but the RHS becomes:

$$F(\boldsymbol{k}',\omega) = \lambda(u(\boldsymbol{k}') + F(\boldsymbol{k}',\omega)) \sum_{k} u^2(\boldsymbol{k})\, G_0(\boldsymbol{k},\omega) = \lambda\, I(\omega)\big(u(\boldsymbol{k}') + F(\boldsymbol{k}',\omega)\big) \quad (2.39)$$

We can re-arrange this in terms of $F(\boldsymbol{k}',\omega)$,

$$F(\boldsymbol{k}', \omega) = \frac{\lambda\, I(\omega)\, u(\boldsymbol{k}')}{1 - \lambda\, I(\omega)} \quad (2.40)$$

We can plug equation 2.40 into equation 2.37 to find a compact equation for $T(\boldsymbol{k}, \boldsymbol{k}', \omega)$;

$$T(\boldsymbol{k}, \boldsymbol{k}', \omega) = \lambda\, u(\boldsymbol{k}) \left(u(\boldsymbol{k}') + \frac{\lambda\, I(\omega)\, u(\boldsymbol{k}')}{1 - \lambda\, I(\omega)} \right) \quad (2.41a)$$

Which simplifies to…

$$T(\boldsymbol{k}, \boldsymbol{k}', \omega) = \frac{\lambda\, u(\boldsymbol{k}) u(\boldsymbol{k}')}{1 - \lambda\, I(\omega)} \quad (2.41b)$$

We can use the zeroes of the denominator of this equation to find the energy of each bound state.

We can write the transmission ratio in terms of the incident electric fields as follows:

$$t(\omega_j, \omega_k) = \frac{E_t(\omega)^2}{E_{pr}(\omega)^2} \quad (2.42)$$

Where the subscript pr refers to the probe beam (and subsequently, the subscript p will refer to the pump beam), and t refers to the transmitted laser. We can rewrite the numerator similarly to equation 2.03 in terms of the linear and non-linear polarization:

$$t(\omega) = 1 - \frac{4\pi\omega}{nc} \frac{Im\left[E_{t,0}\left({P^{(1)}}_t(\omega) + {P^{(3)}}_t(\omega)\right)\right]}{E_{pr}(\omega)^2} = \frac{T + DT}{T} \quad (2.43)$$

Where the imaginary portion of the component of the electric field is the absorption, therefore we can define transmission as the difference between the absorption and unity. We can rewrite $\frac{DT}{T}$ in terms of the non-linear susceptibility:

$$\frac{DT}{T} = -\frac{4\pi\omega}{nc} \frac{Im\left[E_{t,0}\left(\chi^{(3)}(\omega) {E_t}^2(\omega)\right)\right]}{E_{pr}(\omega)^2} \quad (2.44)$$

We can evaluate our nonlinear susceptibility $\chi^{(3)}(\omega)$ as a sum of the signal contributions of the contribution of each particle:

$$\chi^{(3)}(\omega_{pr},\omega_p) = -\sum_{i,j=ex,tr}\left(\frac{\chi_i{}^{(1)}(\omega_{pr})}{\mu_i}\right)^2\left(\frac{\chi_j{}^{(1)}(\omega_p)}{\mu_j}\right)^2 T(0,0,\omega) \quad (2.45a)$$

$$\mu_{ex} = \mu \quad (2.45b)$$

$$\mu_{tr} = f\sqrt{n'} \quad (2.45c)$$

$$\chi_{ex}{}^{(1)}(\omega) = \frac{\mu^2}{\hbar\omega - \epsilon_{ex} + i\gamma_{ex}} \quad (2.45d)$$

$$\chi_{tr}{}^{(1)}(\omega) = \frac{f^2 n'}{\hbar\omega - \epsilon_{tr} + i\gamma_{tr}} \quad (2.45e)$$

Where the subscripts refer to the response from the exciton and trion, μ refers to the exciton dipole moment, γ refer to the linewidth of the signal, ϵ_i refers to the energy of the particle in the subscript, and f refers to the amplitude of the trion exciton, n' refers to the doping density of the sample.

To describe the interactions in our system, the T-matrix is a 4 x 4 matrix to account for two parameters: the species (exciton and trion) and the valley polarization $(+,-)$, meaning the possible states in this configuration are $++,+-,-+,--$ for the exciton-trion spin states. Many of our squared terms, as a result, involve spin-mixing processes due to each diagonal element referring to such. Note that this chapter covered only the cross-circular excitations, however using the full matrix model, we can evaluate a linear excitation in terms of a sum of the two co-circular channels $(++,--)$.

Conclusion

In this chapter we have established some of the effects we can observe from non-linear optical processes, defined non-linear optical processes as a function of susceptibility, then formed a 2-level model whose arguments can be extended to a 4-level model, so that we can model the non-linear processes occurring within the nonlinear optical system.

Chapter 3 - Sample Fabrication

High quality 2D heterostructures can be formed using a process involving mechanical exfoliation[60] characterization, and dry transfer to stack the layers on top of one another with high-accuracy lattice alignment to create moiré heterostructures[61]. In this chapter, I detail: **1)** the mechanical exfoliation technique commonly used to create single and thin layers of materials, **2)** characterization methods used to examine the quality of exfoliated materials, **3)** the dry transfer method to create 2D heterostructures.

3.1: Mechanical Exfoliation and Searching

The simplest method to finding isolated, thin, and high-quality 2D materials is the mechanical exfoliation technique using Scotch tape. We can isolate layers by using the property of SiO_2 where the van der Waals force between SiO_2 and a thin layer of material is greater than the force between two layers of material.

Figure 3-1. Bulk Crystals of WSe_2 used for exfoliation.

The process of exfoliation involves taking a small piece of a larger bulk crystal and placing that crystal on tape. The bulk crystals are several microns thick and grown in at Oak Ridge National Laboratory/University of Tennessee.

We then place a small 0.5 mm x 0.5 mm piece of bulk crystal onto a piece of Scotch tape, and repeatedly fold and unfold the scotch tape in such a way to both avoid crystal overlap and to form

large crystal spots as shown in Figure 3-2. Doing this limits the excess tape residue due to a second tape touch. This allows the sample to remain high quality, which we later characterize in Section 3-2.

Figure 3-2. Exfoliation pattern on scotch tape, with many large crystal spots.

The tape in Figure 3-2 is delicately placed on a chip with a thin film of SiO_2 on a piece of Silicon. The thin film of SiO_2 is either 90 or 285 nm in thickness; this does not affect the van der Waals interaction between the bulk on the tape and the SiO_2, however it changes the appearance of the sample when viewed under an optical microscope. The placement of the tape and its interaction with the SiO_2 most directly affects the quality of the crystals on the chip, and they are placed in contact with the weight of a light pair of tweezers.

Then, we place the chip onto a hot plate set to 100°C for two minutes; this expands the tape and the chip and places them into light contact with one another. Afterwards, when it is taken off the hot plate and given time to cool, the tape naturally peels off slightly due to a cooling effect, and then we slowly pull the tape off the chip, by pushing the chip down and pulling up on the tape simultaneously until the tape is removed. Afterwards, we can observe the transfer of bulk directly onto the chips, as seen in Figure 3-3.

Afterward, the samples can be found by systematically searching through the chip with a Nikon optical microscope at varying magnifications. Each material has a different optical profile in terms of color at different thicknesses; the TMD materials we discuss in this thesis show up as a translucent purple as shown in Figure 3-3. Graphene shows up as a lighter shade of purple, and hBN shows up at various degrees of blues and greens at various low thicknesses. This is due to thin-film interference effects between the SiO_2 and the thin layer of material. For hBN, we can more easily observe pieces less than 2 nm thick using 90 nm SiO_2, however we use 285 nm SiO_2 for TMDs and Graphene.

Figure 3-3. WSe_2 exfoliated onto 285 nm thick SiO_2 on Si. The areas with more visible crystals are more likely to contain monolayers since that is where the bulk crystals have made contact.

Due to the properties of each material, the various steps require small differences depending on the material. For instance, Graphene does not have as strong a propensity to stick to SiO_2 chips as TMDs and hBN, meaning that we often use significant amounts of bulk to create a tape and we use significant force to transfer between the tape and the chips. TMDs are relatively brittle in comparison and requires significantly less bulk that is more spread out and isolated.

3.2: Characterization Methods

The thickness, angular orientation, and topological cleanliness of a sample can be characterized using Photoluminescence (PL), Second Harmonic Generation (SHG), and Atomic Force Microscopy (AFM). These are used in conjunction to create high quality heterostructures by identifying samples and ensuring surface purity when creating heterostructures. In this section, I briefly discuss optical characterization results used to identify the thickness of the sample as well as the angular orientation of a TMD and how we use the AFM to check the topology of the sample.

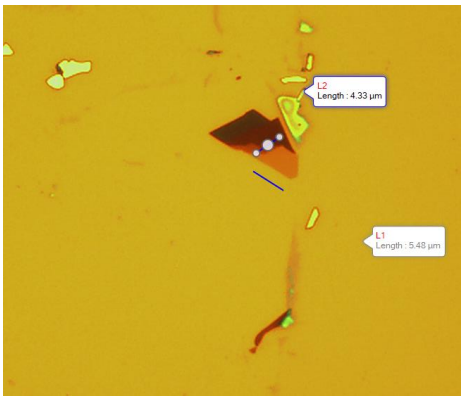

Figure 3-4. 100x optical image of WSe_2 monolayer on 285 nm SiO_2. The monolayer portion appears as a translucent purple color, with extra layers of WSe_2 being a darker shade of purple as shown by piece directly to the left of the monolayer. The yellow pieces are bulk WSe_2 which are on the order of hundreds of nm thick. Note that $MoSe_2$ follows a similar color convention.

3.2.1: Optical Characterization

As show in Chapter 1, as TMD semiconductors become thinned from bulk to monolayer, the band gap goes from indirect to direct. This can be measured this at room temperature with a PL setup which I will describe in more detail in Chapter 4. We can identify a monolayer of material by whether it produces a strong exciton signature. The signal in Figure 3-5 is an exciton resulting from a WSe_2 monolayer excited by a 20 µW green (λ = 532.8) or red Helium-Neon (λ = 633 nm) laser. The back radiation from the TMD is then collected into a .8 NA objective, filter and sent into a spectrometer with a center wavelength at 750 nm, and a 1 second exposure time. If a clear PL signal is detected, then this sample is a monolayer.

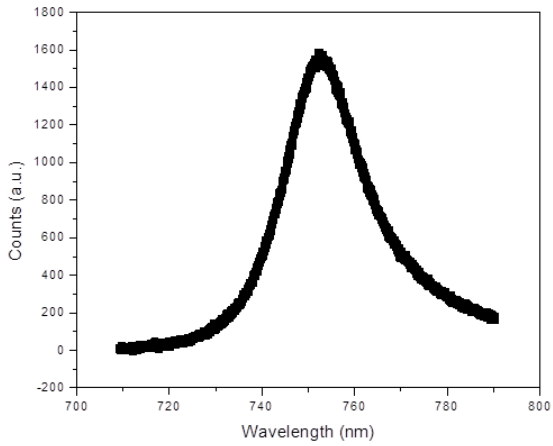

Figure 3-5. Background corrected PL Spectrum of monolayer WSe_2. showing a strong PL signal at λ = 754 nm. This bound exciton signal does not exist for other TMD semiconductor thicknesses.

We follow this with SHG to determine the crystal axis orientation of the TMD. SHG involves a process using a polarized, 1 mW, pulsed laser with λ = 800 nm. The sample emits a signal at λ = 400 whose strength depends on the light polarization axis relative to the TMD crystal axis[62]. This is a second order nonlinear effect observed in semiconductors which results in frequency doubling, often used to measure the orientation of a molecule[63–65].

Figure 3-6a shows the optical image of the sample in the SHG optical setup, which is hit by the incoming pulsed laser. Figure 3-6b shows the resulting sinusoidal response as a function of polarization, which is then fit to Equation 3.01:

$$y = y_0 + A \sin^2\left(\frac{\pi\,(x - x_c)}{w}\right) \quad (3.01)$$

where x_c refers to the relative phase angle in degrees, $w = 60°$ is the rotational period of the lattice, and x refers to the relative polarization angle of the incoming pulsed laser. By measuring x_c between two separate monolayers using the same relative orientation of the incoming laser, we can align these monolayers later with high accuracy lattice-matching.

Additionally, we can perform Raman spectroscopy on Graphene to determine the thickness of a piece of Graphene; this can identify a monolayer with great accuracy[66]. This process involves the comparison between the relative magnitude of two vibrational modes of Graphene[67] when the vibrational modes are excited by a relatively high-power (approximately 500 μW) beam.

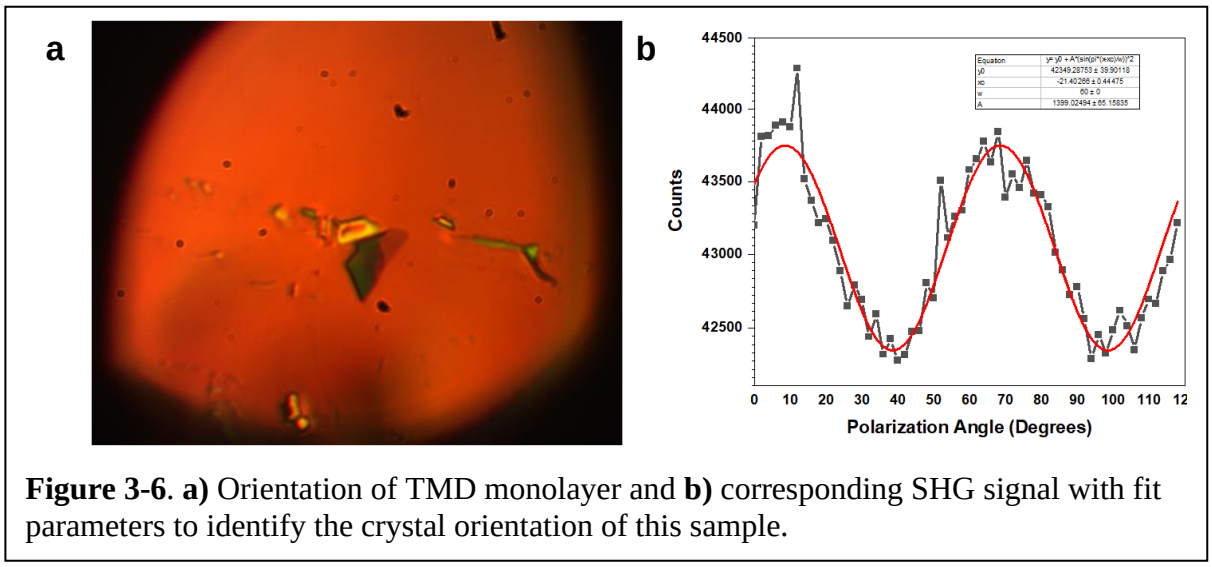

Figure 3-6. **a)** Orientation of TMD monolayer and **b)** corresponding SHG signal with fit parameters to identify the crystal orientation of this sample.

3.2.2: Atomic Force Microscopy

AFM is a characterization technique which is used to probe the topological cleanliness of the sample and its subsequent heterostructure. We use a Park AFM system to image the samples by directing an atomically thin tip to interact with the sample and measure the height of the sample as a function of space[68]. This provides high-resolution imaging of a sample and assess its cleanliness to prevent noise from localized charge effects and interactions with unknown residues.

Figure 3-7 shows an optical image of hBN (a) and its corresponding AFM image (b). The AFM image can be analyzed in many ways, either to provide line profiles or to average heights over a certain region as shown in (c). AFM is important for imaging the thickness of hBN.

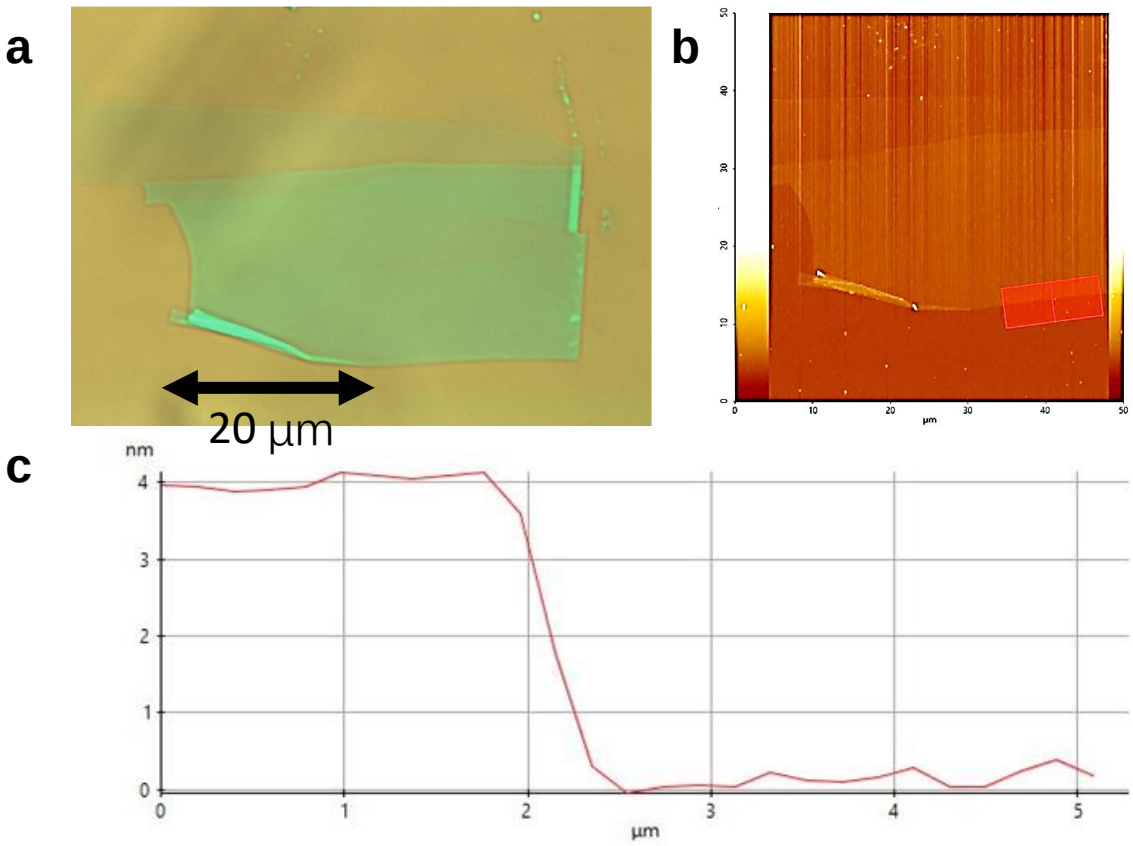

Figure 3-7. A standard AFM procedure on a piece of hBN. **a)** The optical image of a piece of hBN, **b)** its corresponding AFM image, and **c)** the line profile average over the red box on b. This shows that the piece of hBN is around 4 nm thick.

Figure 3-7 shows the ideal cleanliness of an exfoliated material. There are often small features which appear on the AFM which are absent from the optical image; these often fail to show up due to the significantly higher imaging resolution of AFM compared to optical images. However,

in the case of the piece in Figure 3-7, there is very little untracked residue between the optical image and the AFM.

3.3: Dry Transfer Method

After characterization, we can stack these materials using a dry transfer method. Materials are stacked and orientated to lattice-match and insulate a portion of TMD materials from the environment. This dry transfer method utilizes the van der Waals force between materials to create heterostructures by using a thin film to peel the samples from the substrate, using a microscope and a stamp connected to a micrometer. These two in conjunction allow us to precisely align samples to great precision.

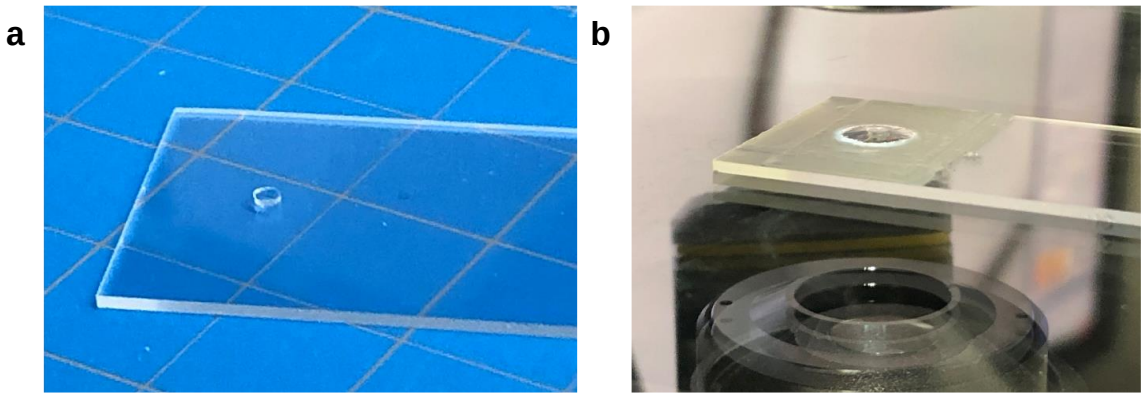

Figure 3-8. A PDMS stamp **a)** before the PC film is placed on top of the PDMS and **b)** after.

The first step to creating heterostructures is to create a stamp to facilitate the transfer between materials. The stamp consists of a block of polydimethylsiloxane (PDMS) (Figure 3-8a) on a glass slide with a polycarbonate film draped over top of it. This simultaneously puts pressure on the film and stretches the film out tightly so the film does not move during the transfer process. A sample

stamp is shown in Figure 3.8b. We anneal the PC onto the PDMS by baking it on a hot plate at 175°C for two minutes; this is to remove as many air pockets and impurities as possible to ensure the cleanest transfer and the flattest film.

The stamp is then mounted upside-down onto a magnetically mounted arm with micrometers to move the stamp. Then, middle of the stamp is placed underneath the microscope and positioned over the top of the sample. Typically, the first material picked up is hBN due to its strong van der Waals attraction to the PC film and various other 2D materials.

Upon locating the hBN, sample is pre-heated to 50°C then touch down gently and lightly onto the vicinity of the sample as shown in Figure 3-9, using a clean part of the stamp. From there, the sample-stamp system is heated up slowly to 90-100°C (at a rate of 2°C/s) until the film is draped over the sample and 20-25 μm beyond the sample.

The temperature is then decreased slowly to 50°C again. This causes the PC film to “peel” off the sample slowly, to prevent various cracks and defects from pressure. When the sample reaches reach 50°C, the stamp is lifted off the substrate to prevent any excess strains and resulting cracks on the picked-up sample. This process is used to pick up any piece onto a substrate.

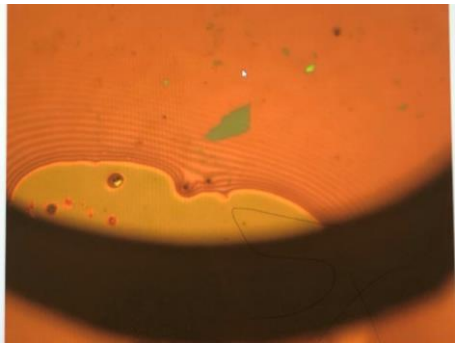

Figure 3-9. A stamp lightly touched down near the target piece, in this case a piece of hBN. The dark yellow part is where the stamp contacts the chip, and as the temperature rises the contacted portion expands slowly over the top of the sample.

To align a sample on the PC film with a sample on a substrate, the stamp is moved slowly downwards towards the substrate and switch the focus of the microscope between the stamp and the substrate. We continue to adjust the alignment between the two samples until the stamp and sample are close enough in contact where both the PC surface and the sample are both focused on the same image, but the stamp is not yet in contact. Once this happens, it is safe to touch the stamp down so long as the two samples are not in contact. The slow thermal expansion allows the two samples to touch without displacement so long as there are no external shocks to the system.

To make moiré heterostructures, we use phase results from SHG measurements in Figure 3-6 to adjust the angular orientation of the sample. Then the heterostructures are aligned at an angle such that their orientation relative to one another is at 0 degrees or a multiple of 60. This precision is achieved by using image crop and rotation software to rotate TMDs to a certain angle and stack their images over one another. We use Microsoft Powerpoint to facilitate the crop, rotation, and stacking the aligned sample images on top of each other.

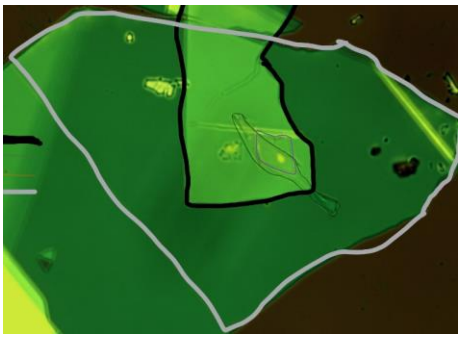

Figure 3-10. A $MoSe_2$-WSe_2 (purple and black respectively) lattice-aligned heterostructure encapsulated between two thick pieces of hBN (light gray and black). There are some remnants such as dirt in the middle of the contact area in the heterostructure, however both TMDs are accurately lattice matched.

Various desktop computer tools (such as EpicPen) are also used to trace the image of the stack and align the optical image underneath the stamp to the stack image.

Then, the final heterostructure-on-PC system is melted onto stamp onto the target substrate – examples of such substrates include patterned SiO_2 chip, a regular SiO_2 chip, another sample, or a Sapphire substrate. The melting process places the stamp with the full sample into contact with the target substrate, and then the system is heated to 200°C, which is above the melting point of PC. After reaching the melting point, we slowly raise the arm up and the heterostructure is now on the final substrate. Figure 3-10 shows the optical image of an hBN-$MoSe_2$-WSe2-hBN heterostructure on Sapphire after removing the PC film.

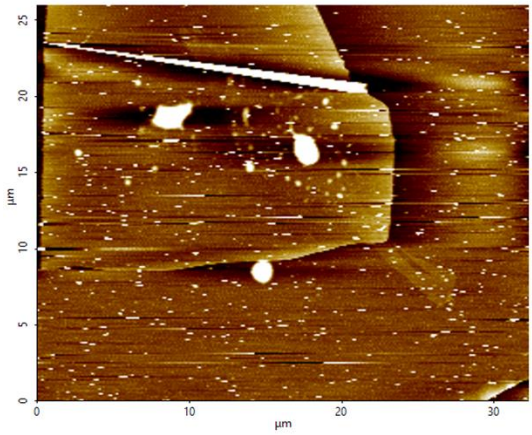

Figure 3-11. Corresponding AFM scan of transfer from Figure 3.9. There is dirt between the layers but also there is much noise caused by small amounts of dirt from the transfer process. The bright white areas are spots that are significantly taller than the focused heterostructure area.

The film is removed by placing the sample in a chloroform bath for 20 minutes followed by an IPA bath for 10 minutes. We also perform AFM after the transfer to check any trace amounts of PC film and any air gaps that may result from a transfer (Figure 3-11). There are various methods to remove these small air gaps and dirt fillings; among these are a "nano-squeegee" method[69] which physically pushes dirt and air gaps out using an AFM tip in contact mode, as well as annealing at 320°C in an inert gas chamber[70].

After applying on these processes and performing the final characterization through the AFM, we can utilize EBL to create macroscopic gold contacts to perform optoelectronic measurements.

3.4: Electron Beam Lithography

Electron Beam Lithography (EBL) is a method used to create electrical contacts onto our sample to contact to metals[71], create plasmonic substrates to observe plasmons in TMD semiconductors[72–74], and creating vacancies for finely etching graphene[75,76]. The basis behind EBL is to selectively alter a resist film onto our sample by using a Scanning Electron Microscope (SEM) to "carve" out a pattern in the resist determined by a CAD software. We can then deposit a thin conductive film onto our sample through thermal evaporation and remove the excess conductive film on resist. Afterwards we can wire-bond our sample to an optical cryostation mount which can then be connected to a power supply or a multi-meter to perform opto-electronic measurements.

3.4.1: PMMA & Nanopattern Generation on Conductive Substrates

We start our EBL process by spin-coating 495 A4 PMMA onto our sample for 60 seconds at 2000 rpm, then placing our sample on a hot plate set to 160°C for two minutes. This ensures that the PMMA layer is spread evenly through the sample creating an even 200 nm thick layer on the sample. The hot plate anneals the PMMA onto the sample. After the sample cools, 950 A4 PMMA is spin-coated onto the sample for 60 seconds at 2000 rpm (300 nm thick layer), then placed onto the hot plate again at 160°C for two minutes. We then take a 50x optical image of the sample for

both alignment and to show features. A sample device with both layers of PMMA coating is shown in Figure 3-12.

Another key feature of Figure 3-12 are the alignment markers (two gold squares overlapped at the corner) and coordinate markers (larger grids of gold patterns). The alignment markers are spaced 25 µm apart with coordinate markers placed 100 µm apart. Each row of a coordinate number corresponds to a two-digit number, with each character representing a single number (Figure 3-12). In Figure 3-13, we show the CAD software with various boxes, markers, and patterns on an optical image of graphene-gated/contacted sample (using three contacts). In our standard EBL procedure, we place four unobtrusive alignment boxes around the sample and assign a central coordinate marker (typically the nearest unobtrusive coordinate marker to the sample). We note that we set one edge of our sample to be perfectly straight to ensure consistency between our intended pattern, the CAD file, and the optical image.

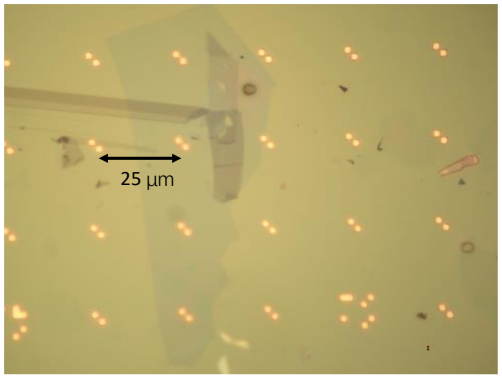

Figure 3-12. Device spincoated with two layers of PMMA. The two boxes connected at the corners are alignment markers and approximately 25 µm apart, whereas the larger clusters of patterns are coordinate markers which appear every 100 µm in the x and y directions.

The pattern uses three separate layers with varying degrees of precision. Figure 3-13b shows that there is a pattern connected directly to the sample (Layer 4), which is then connected to an intermediate pattern (Layer 5) that is connected to a larger square (approximately 1 µm × 1 µm)

(Layer 6). Using the run file, we can customize the spot size, magnification, and electron beam density in accordance to the precision necessary for a particular layer. Layer 4 has the lowest spot size, highest magnification, and lowest electron area dosage density from the electron beam for high precision, whereas Layer 6 has the highest spot size, lowest magnification, and highest electron area dosage density.

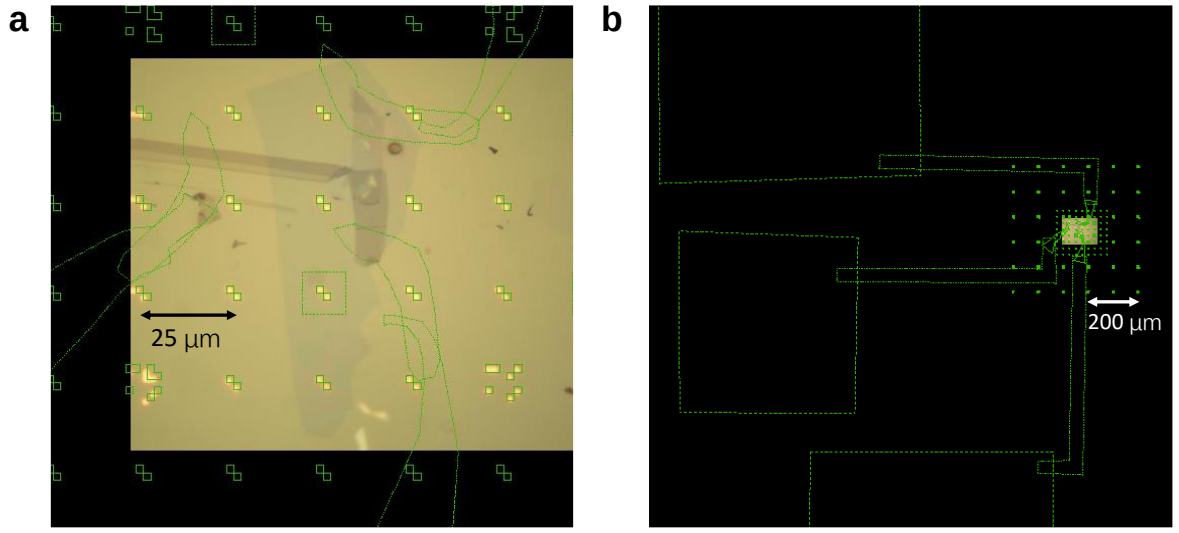

Figure 3-13. Sample CAD software showing precise alignment of alignment boxes and coordinate boxes within the software. **a)** Shows the high precision pattern (Layers 4 & 5). There are four specific alignment markers chosen to be the central alignment markers which are noted by a box. The central coordinate marker for this device is chosen to be the top right due to its distance from the precise patterns. **b)** Shows the low precision / high area pattern (Layer 6), showing the schematic of the larger electrical pads in the software.

When the pattern is created, re-centered, and simulated on the Nano-Pattern Generation System (NPGS) software, we can perform the EBL in the SEM. The sample and a faraday cage are both loaded into the SEM at the *W.M. Keck Center for Nano-Scale Imaging.* Current is measured by centering the SEM image onto the faraday cage, and measuring the corresponding current for each spot size, which is then recorded onto the CAD run file. Afterward, we move the SEM image to

the physical position of our sample, with standard spot size and large magnification to prevent potentially intrusive patterns from being written into the resist. We start by straightening the edge to stay consistent with our pattern, then process the run file.

The run file starts by asking for points to calculate the equation of the plane of the substrate. This is done by recording two to four different focused points on the substrate; the software records the X, Y, and Z values and attempts to model the substrate using the entered coordinates. Then we can search for our central coordinate, first by finding any numerical coordinate and then using the distance between numerical coordinates to precisely navigate to the center coordinate without unnecessary writing into the PMMA. Afterwards, we execute our run file after processing it and the pattern is written after a short alignment step. Afterward, the sample is placed in MIBK to develop the pattern created by the SEM.

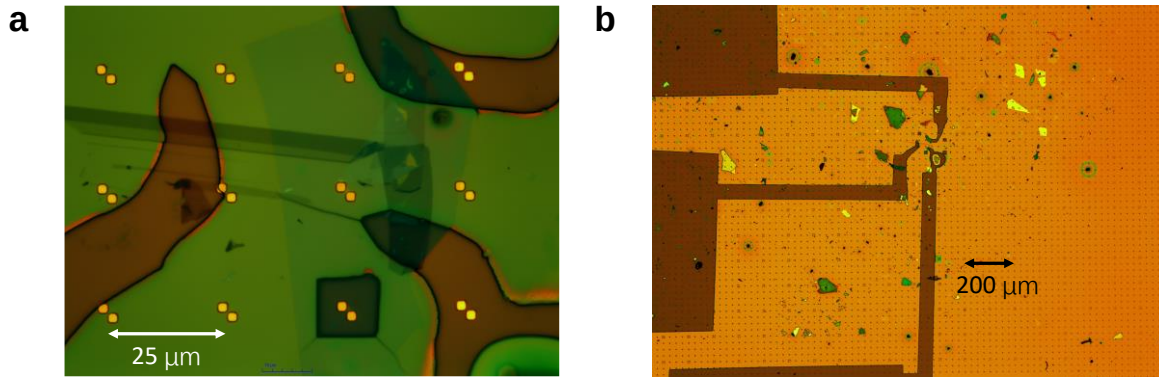

Figure 3-14. Optical image of a pattern with PMMA after development at **a)** 100x magnification, showing the development of the finer features and **b)** 5x magnification, showing the development of the larger features.

3.4.2: Thin Film Deposition

Figure 3-14 shows an optical image of a pattern with PMMA after development, where there are clear vacancies in the film consistent with the pattern in Figure 3-13. Figure 3-15 shows a side-view of the film after development and evaporation, where the lower layer of PMMA is more developed than the upper layer of PMMA. This is because the lower layer is more susceptible to writing due to being an overall thinner film. We then place the sample in a thermal evaporator, which also allows us to measure the precise thickness of deposited film, starting by evaporating 5 nm of chrome (as a sticking layer) as followed by 30 nm gold.

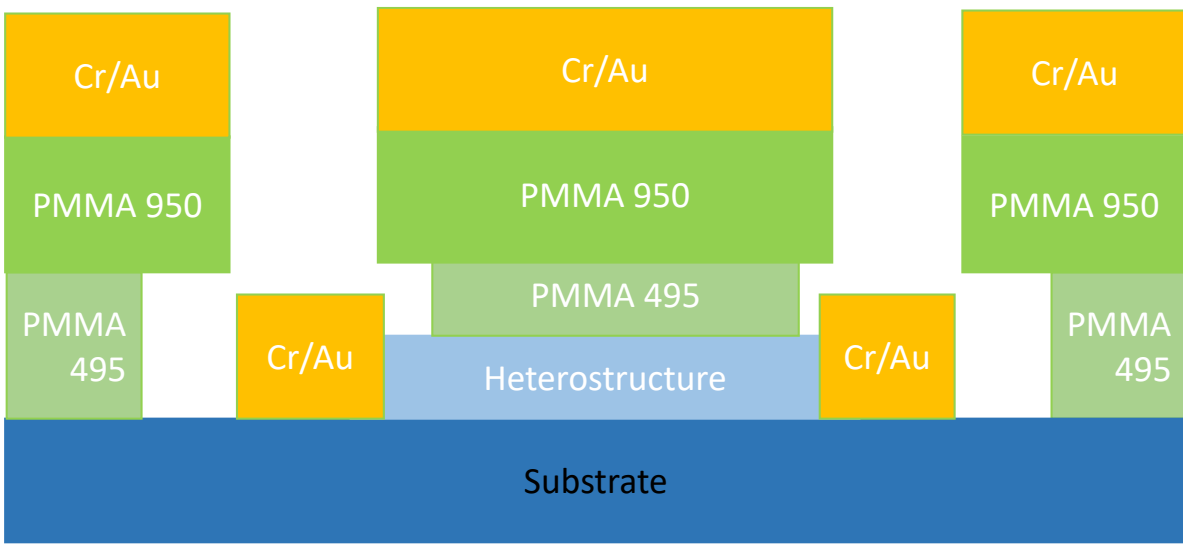

Figure 3-15. Side-view of a sample after the EBL and evaporation process. There are small gaps between the Cr/Au alloy and the PMMA, as well as Cr/Au on top of PMMA. The small gaps allow us to wash the PMMA away and anything about the PMMA (including excess Cr/Au).

The small gap shown between the two layers of PMMA allows for the removal of excess PMMA and deposited thin conductive film. The PMMA is removed from the substrate using physically pulsed acetone, which is then washed in IPA. Figure 3-16 shows the sample after the deposition and lift-off process is completed. Then, the sample can be physically wire-bonded onto a substrate and later placed into a cryostation for various optoelectronic measurements.

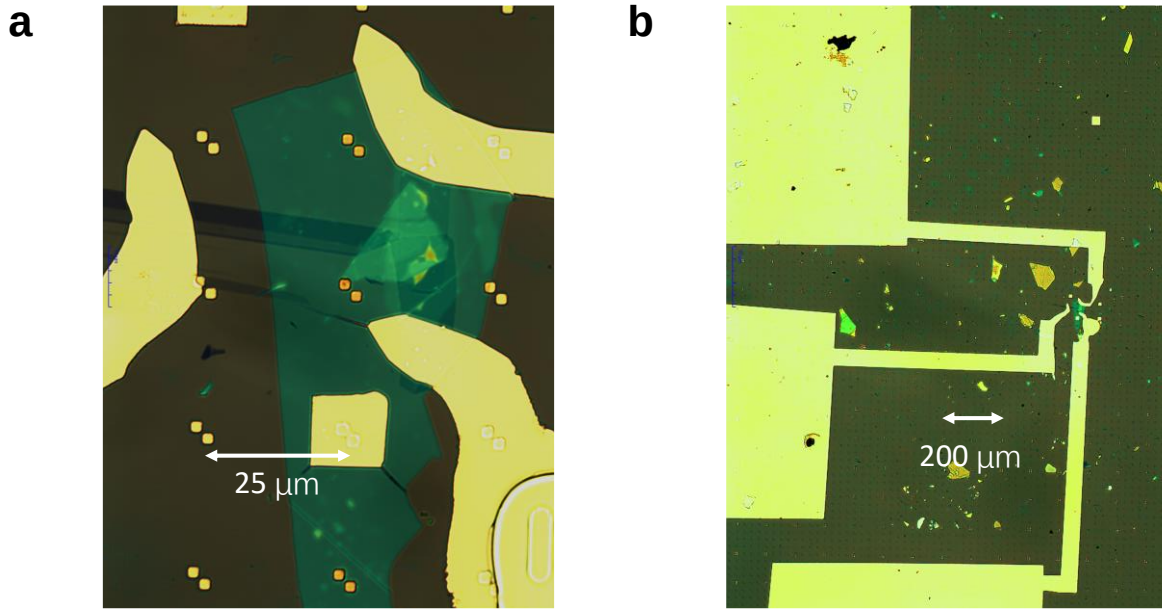

Figure 3-16. Optical image of sample after evaporation and removal of PMMA at **a)** 100x magnification and **b)** 5x magnification.

3.4.3: EBL on Insulating Substrates

One issue with the previous method is that it only applies in the case where the substrate has a conduction layer. In the previous case, the Si underneath the SiO_2 substrate allows for a path for the electrons to disperse and ground. If similar processes are performed on a substrate with no conductive layer, the fidelity of the pattern is immensely reduced due to charges trapped in the

PMMA. The charges trapped in the PMMA create a repulsive force, significantly reducing pattern fidelity.

However, we have developed a method to perform EBL on strongly insulating substrates such as, in our case, c-axis sapphire. The process is fundamentally the same, however we must create our conductive layer on top of the PMMA. We do this by applying a layer of the DisCharge H_20X2 conductive resist on top of the already existing 495 and 950 layers, at 2000 rpm for 60 seconds (100 nm layer). The film is then given time to solidify in air instead of baked onto the substrate. When performing the EBL process at the SEM, the sample is mounted using copper clips which are placed on the "short" side of the sample pattern, to ensure the shortest distance to ground any excess electrons. The electron area dosage density must be adjusted in accordance to equation 3.01:

$$n_{sapphire} = \frac{n_{Si}}{9}(21 - S) \quad (3.01)$$

Where $n_{sapphire}$ is the electron area dosage density inputted into the run file for the sapphire substrate, n_{Si} is the corresponding dosage density for the run file for spot size S on a SiO_2/Si substrate. This is because finer features require many more electrons in order to penetrate the extra layer of resist.

Conclusion

In this chapter, I have shown many methods in which we can fabricate various types of van der Waals heterostructures, and that many of these methods can be generalized to create

heterostructures out of any van der Waals heterostructure. I have also shown how we can form electrical contacts on substrates in both conductive and insulating substrates, for various opto-electronic applications and measurements on complex heterostructures.

Chapter 4 - Optical Techniques

In this chapter, we outline the optical techniques we use to conduct the measurements described in Chapter 5. This chapter details: **1)** sample imaging and alignment, **2)** photoluminescence spectroscopy, **3)** continuous wave (CW) nonlinear spectroscopy.

4.1: Optical Microscope

Figure 4.1 shows a diagram of the imaging portion of a microscope optical setup. The white light source is sent through a 0.65 NA objective lens where it is focused onto the sample and reflected through the original path. A 50/50 beam splitter reflects the image onto the camera with a 10-20mm lens, resulting in a magnification of ~50 times. We can mechanically adjust the position of the substrate to find our sample, either with a standard three-axis mechanical stage or using piezo-electronic controllers.

In our experiments, the laser source (used to excite or probe the sample) is often a green (532 nm) diode laser, a red (633 nm) Helium-Neon gas laser, or a (700-1000 nm) Ti-Sapphire laser. The dichroic mirror reflects within a specific wavelength and transmits outside of those wavelengths; this mirror is selected on its optimal reflection and transmission frequency and may be replaced by a 50/50 beam splitter if necessary. Both the laser and the white light source are focused onto the sample and reflected through the white light source's original path, which is then focused onto the camera and allows us to view an image of the substrate. The sample is placed on either a room temperature stage or is housed inside of an optical cryostat with piezo electronic positioners. The pellicle beam splitter is on a flip mount so that this setup can easily switch between imaging and

spectroscopy modes (changing between Figures 4-1 and 4-2/4-3) after aligning the beam with the sample.

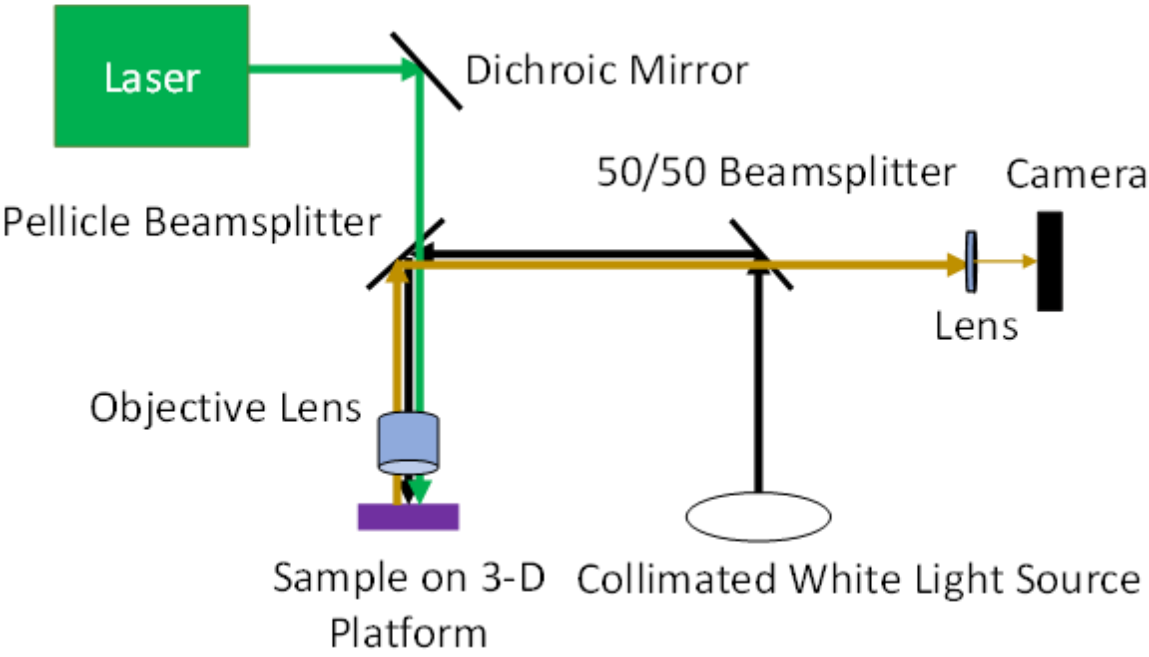

Figure 4-1. Diagram of an optical microscope in our optical setups. The black and green lines represent the path of the collimated white light source and the excitation source, respectively. The gold line represents the reflection of both the excitation source and the collimated white light source from our sample.

4.2: Photoluminescence

Photoluminescence (PL) is the resulting light emitted by a sample following excitation by an external source of light. PL measurements are often used to study direct band-gap semiconductors, which efficiently emit light (see Chapter 1). Figure 4-2 shows a diagram of our PL setup.

We use a laser with higher excitation energy than the sample's band gap to create electron-hole pairs which relax to form excitons. The path of the laser includes a variable neutral density (ND) filter to adjust beam power, as well as the appropriate choice between a beam splitter and a dichroic mirror. A dichroic mirror is preferred for PL setups because they have a narrow reflection band and a broad pass band. For instance, the dichroic mirror we use with our green laser has a narrow reflection band around 532 nm (2.33 eV), but a broad pass band above 700 nm (1.77 eV). This is optimal with TMDs such as WSe_2 and $MoSe_2$ because both materials have a band gap above 700 nm (below 1.77 eV), which allows us to reflect the radiation along the same path as the laser, while minimizing any residual laser reflections.

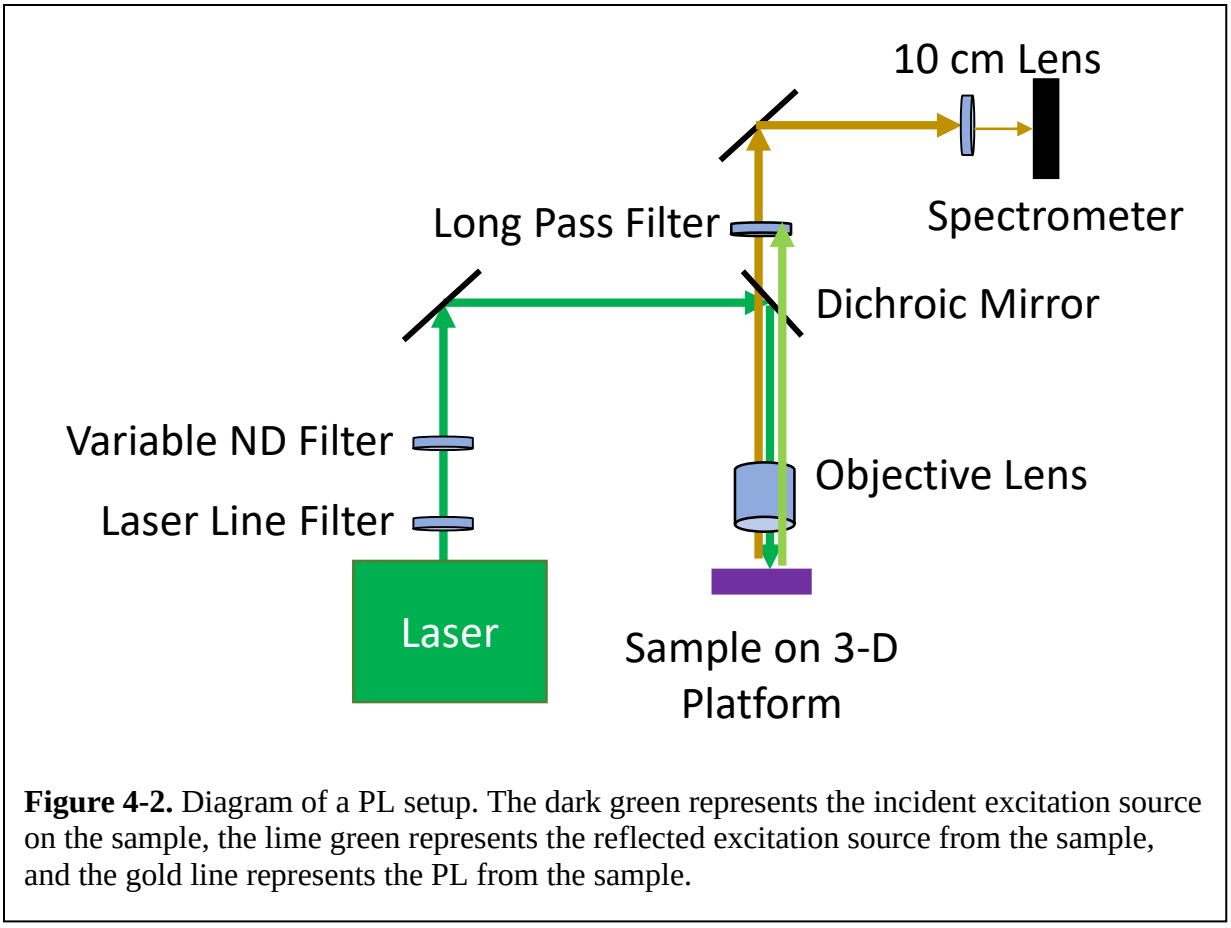

Figure 4-2. Diagram of a PL setup. The dark green represents the incident excitation source on the sample, the lime green represents the reflected excitation source from the sample, and the gold line represents the PL from the sample.

The sample spontaneously emits a photon after the electron and hole recombines. The PL is collected by the objective lens and sent back through the original path of the laser. The transmitted portion of the beam splitter is then sent through a long pass filter and focused onto the entrance slit of a spectrometer. For our experiments, this long pass filter prevents anything below 700 nm from passing thereby blocking any remaining incident radiation from the excitation source. The light is dispersed by a single grating spectrometer and detected with a cooled CCD camera (Andor).

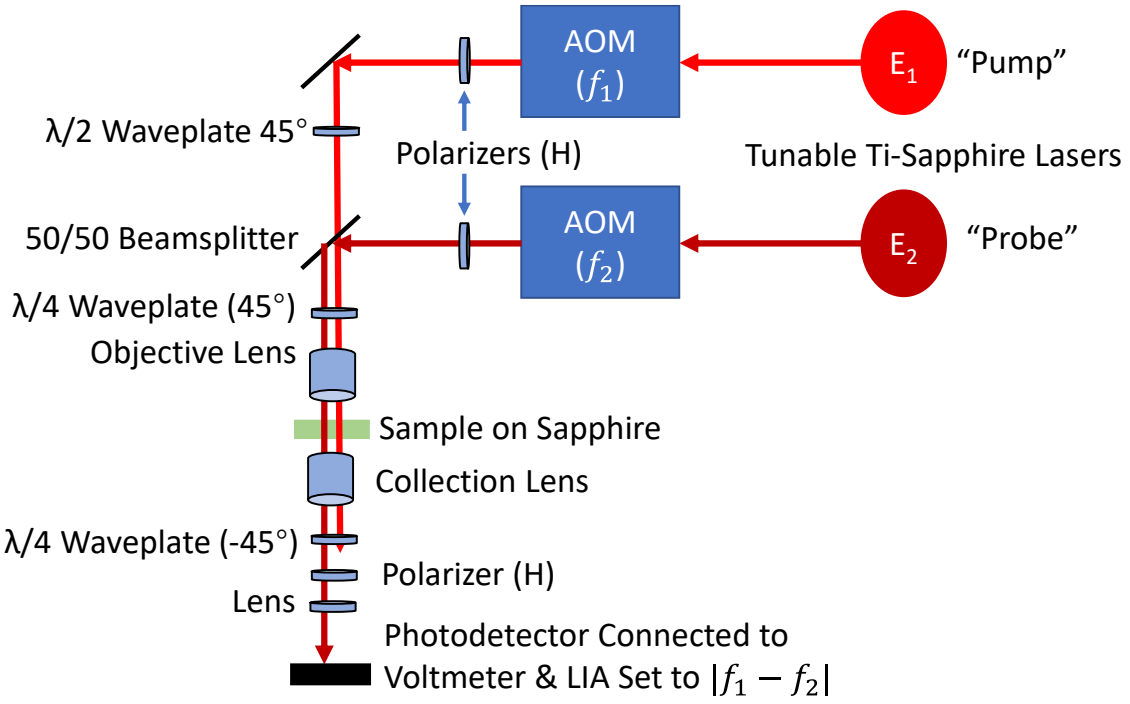

Figure 4-3. Truncated CW Nonlinear spectroscopy diagram. The pump is shown to be filtered out at the polarization analyzer. The photodetector measures the pump-induced change to the probe signal as a result. We can remove the quarter-wave plates to use linearly polarized excitation lasers.

4.3: Continuous Wave Nonlinear Spectroscopy

TMDs have very strong nonlinear optical effects which we can probe through continuous wave (CW) pump-probe nonlinear resonance spectroscopy[77–81]. In Chapter 3, we discussed the nonlinear properties of TMDs. Figure 4-3 shows the setup used for the nonlinear spectroscopy measurements.

The sample imaging system is the same as shown in Figure 4-1, However, in nonlinear spectroscopy, the incident radiation is variable in wavelength and power. Both beams are CW beams which are focused into two acousto-optic modulators (AOMs) using a 50 mm lens.

4.3.1: Acousto-Optic Modulators

A diagram of an AOM is shown in Figure 4-4. Our AOMs utilize a TeO_2 crystal which is supplied with a 200 MHz radiofrequency (rf) signal from an external driver. This signal's intensity is adjusted with an external function generator and drives vibrations in the crystal. When light is incident at the Bragg angle θ_b of the material, the output light is then diffracted at an angle θ according to equation 4.01[82]:

$$\theta = \frac{\lambda f_{rf}}{v_a} = 2\theta_b \quad (4.01)$$

Where λ is the wavelength of the incident laser, f_{rf} is the frequency of the radio signal from the driver (200 MHz), and v_a is the acoustical velocity of our crystal (~4.2 $\frac{mm}{\mu s}$). For our laser wavelength ranges (roughly 740-780 nm) incident into the crystal, we require a θ_b of

approximately 35 – 37 milliradians resulting in a diffraction angle of approximately 17.5 – 19.5 milliradians. The intensity of the diffracted light is described by equation 4.02:

$$\frac{P_d}{P_i} = Sin^2\left(\frac{\pi}{2}\sqrt{\left(\frac{2\,L\,M_2\,P_{rf}}{\lambda^2 H}\right)}\right) \quad (4.02)$$

Where $\frac{P_d}{P_i}$ is the diffracted power efficiency, L (2.5 mm) and H (.32 mm) are the cross-sectional dimensions of the active portion of the crystal relative to the electrodes, M_2 refers to the figure of merit of TeO_2 (~793 $\frac{10^{-15}s^3}{kg}$)[83] and P_a refers to the power output of the rf signal (~.1 W). This results in a diffraction efficiency of ~50%-61% for our wavelength range. Diffraction also occurs to multiple orders, with the diffraction angles being integer multiples of 4.01, however the strongest output is the ±1 order diffracted beam, and our laser input is optimized around the most coherent ±1 order output.

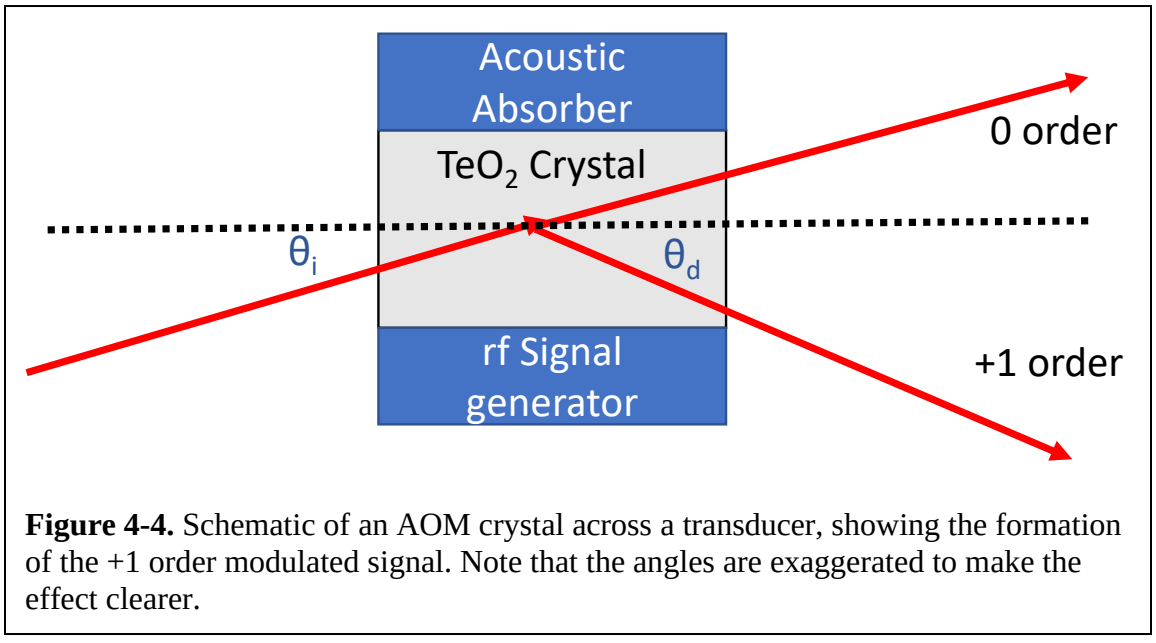

Figure 4-4. Schematic of an AOM crystal across a transducer, showing the formation of the +1 order modulated signal. Note that the angles are exaggerated to make the effect clearer.

The AOM driver is connected to a square wave generator, which determines whether the driver is in the on or off configuration. When the driver is on, there is refraction through the TeO_2 crystal, whereas when the driver is off there is no refraction through the crystal. Our setup uses two phase-locked square wave generators driving two TeO_2 AOMs in an "on/off" configuration.

4.3.2: Continuous Wave Pump-Probe Spectroscopy

In our research, we define two cross-polarized beams as the "pump" and the "probe" and measure our non-linear effects as a change to a probe beam caused by pumping the sample at a certain wavelength. The probe beam is measured by the photodetector at the end of Figure 4.4, whereas the pump beam is filtered out. The pump is modulated with frequency f_1 = 500 MHz and the probe is modulated with frequency f_2 = 553 MHz. These are the "on/off" modulation frequencies of each laser. We use the +1 order diffracted beam from the AOM for the pump and the -1 order diffracted beam for the probe. This reduces the homodyning noise if both lasers are of the same wavelength[84,85].

The signal is then sent through polarizing optics to set the polarization of each beam and focused into a polarization-maintaining fiber. The outgoing polarization is then set so that both outgoing beams are cross-polarized (ie, one is H-polarized and the other is V-polarized). They meet at a beamsplitter and co-propagate to a 0.75 mm objective which focuses both beams onto the sample. In transmission geometry, both lasers move through the sample and are then collected by 12 mm collection lens behind the sample. The transmitted signal is then collimated through a series of wave-plates and polarization analyzers to optimize pump extinction and probe output and focused

onto a photodiode with a 50 mm lens. The photodiode is connected to a lock-in amplifier (LIA) which is set to a frequency equal to the difference in modulation between both AOMs (53 MHz) to measure the difference frequency.

4.3.3: Lock-In Amplifier

The LIA allows us to measure a non-linear signal by amplifying very small signals that occur at a certain frequency. When an electric field is incident on our dielectric sample, it induces a polarization. We can write the photovoltage on the detector as a function of the polarization density as equation 4.03:

$$Photovoltage \sim \left|P^{(1)} + P^{(3)}\right|^2 \ (4.03)$$

Where $P^{(3)}$ is the change in the pump beam due to the probe beam;

$$P^{(3)} = \chi^{(3)}\left|E_p\right|^2 E_{pr} \ (4.04a)$$

And $P^{(1)}$ is the linear polarization term:

$$P^{(1)} = \chi^{(1)}\left|E_{pr}\right| \ (4.04b)$$

Plugging in 4.04 into 4.03 and expanding:

$$Photovoltage \sim \left|\chi^{(1)}E_{pr}\right|^2 + 2\chi^{(1)}\chi^{(3)}\left|E_p\right|^2\left|E_{pr}\right|^2 + \chi^{(3)^2}\left|E_p\right|^2\left|E_{pr}\right|^4 (4.05)$$

Because the nonlinear response is small, we use the highest order $\chi^{(3)}$ term and rewrite 4.06 in terms of beam intensity…

$$Photovoltage \sim \left|\chi^{(1)}\right|^2 I_{pr} + 2\chi^{(1)}\chi^{(3)}I_p I_{pr} \ (4.06)$$

Each beam is modulated at a frequency of $\omega_{p,mod}\ and\ \omega_{pr,mod}$ and phase-matched, so we can rewrite in terms of a cosine function:

$$Photovoltage \sim \left|\chi^{(1)}\right|^2 I_{pr,0} \cos\left(\omega_{pr,mod}t\right) + 2\chi^{(1)}\chi^{(3)} I_{p,0} I_{pr,0}\ \cos\left(\omega_{pr,mod}t\right)\cos\left(\omega_{pump,mod}t\right) \quad (4.07)$$

Which we can rewrite using trigonometric identities…

$$Photovoltage \sim \left|\chi^{(1)}\right|^2 I_{pr,0} \cos\left(\omega_{pr,mod}t\right) + \chi^{(1)}\chi^{(3)} I_{p,0} I_{pr,0} \left(cos\left(\left(\omega_{pr,mod} + \omega_{pump,mod}\right)t\right) + cos\left(\left(\omega_{pr,mod} - \omega_{pump,mod}\right)t\right)\right) \quad (4.08)$$

The LIA allows us to see signals which appear at a chosen frequency. To observe the DT response, we can either have the LIA pick out a signal appearing at the difference modulation frequency ($\omega_{pr,mod} - \omega_{pump,mod}$) or the sum frequency ($\omega_{pr,mod} + \omega_{pump,mod}$). In our measurements, the probe and pump frequencies are 553 kHz and 500 kHz respectively, meaning that probing at 53 kHz or 1053 kHz gives us the pump induced change to the probe signal. In our experiments we use 53 kHz due to limitations of our LIA. The pump induced change to our probe is therefore:

$$DT \sim \chi^{(1)}\chi^{(3)} I_{p,0} I_{pr,0} \quad (4.09)$$

By dividing by the intensity of our probe beam, we can obtain the $\chi^{(3)}$ response resulting from the pump beam:

$$\frac{DT}{T} \sim \chi^{(3)}(\chi^{(1)} I_{p,0}) \quad (4.10)$$

Note that while we do expect higher order terms, they are low in magnitude and oscillate in time. For this reason, we take time averages over ~5-10 seconds to obtain this signal to prevent noise from higher order terms.

We note that we do not expect to see $\chi^{(2)}$ effects due to $\chi^{(2)}$ effects in TMDs being associated with the symmetry of the system, and as a result is dominated by the SHG[64,86]; instead, the response we expect is $\chi^{(3)}$ to the lowest order[12,30,87,88].

Conclusion

In this chapter we discussed our setup for both linear and non-linear spectroscopy. We can image the sample with white light to precisely aim our laser(s). With one laser, we can perform photoluminescence spectroscopy using a dichroic mirror/beam splitter and a spectrometer, used to characterize the sample according to Chapter 3. With two lasers, we can isolate non-linear optical signals by measuring the change to a probe laser caused by a pump laser. We can isolate this signal by setting the frequency of the LIA to the difference in modulation frequency between the pump and the probe lasers.

Chapter 5 - Steady State Non-Linear Spectroscopy on Monolayer $MoSe_2$

In this chapter, I describe nonlinear pump-probe spectroscopy measurements performed on MoSe2 identifying steady state phenomena, and analyze multiple models to explain the signal. We begin by theorizing that we have found a bound exciton-trion biexciton, however we later use a robust T-matrix model to analyze the various interactions contributing to our lineshapes. We use our pump-probe modulation technique from Chapter 4 on a hBN-MoSe2-hBN heterostructure and measure the differential transmission (DT/T) signal from the monolayer.

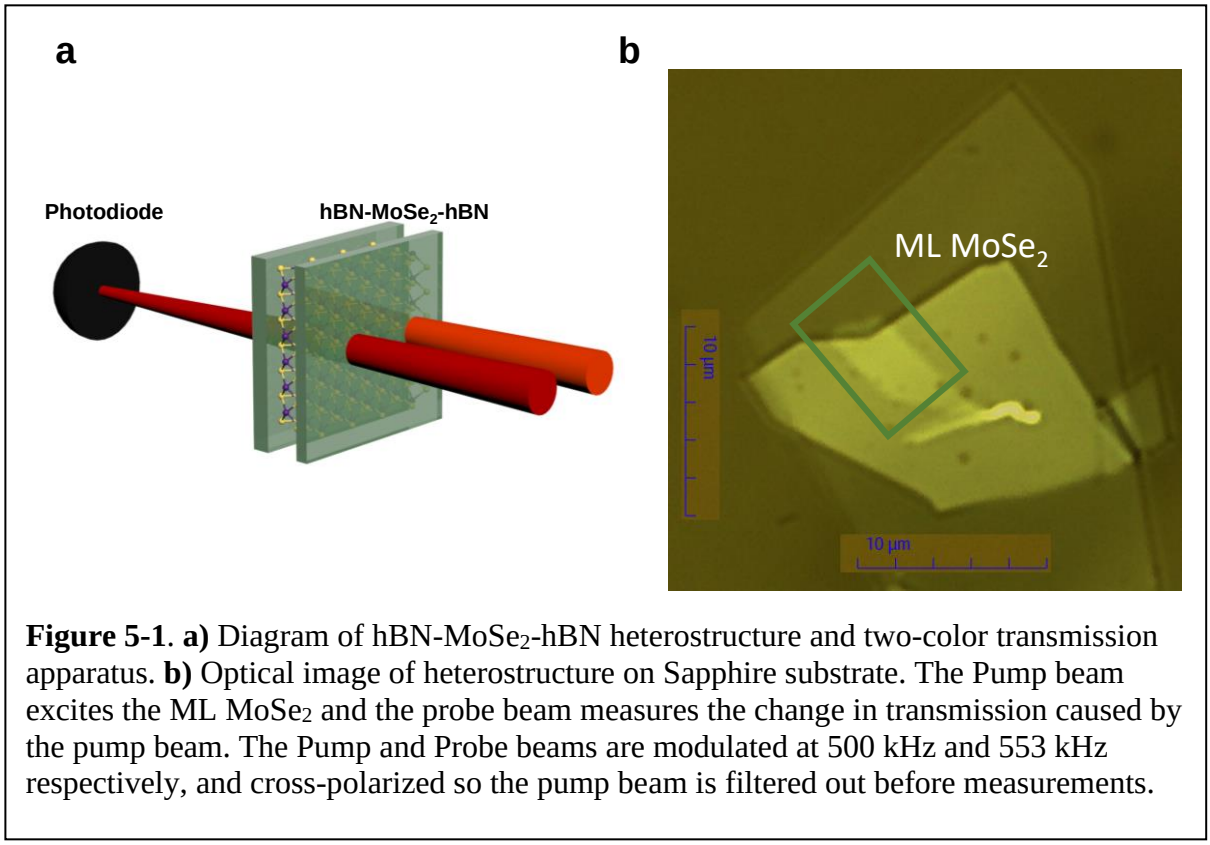

Figure 5-1. **a)** Diagram of hBN-$MoSe_2$-hBN heterostructure and two-color transmission apparatus. **b)** Optical image of heterostructure on Sapphire substrate. The Pump beam excites the ML $MoSe_2$ and the probe beam measures the change in transmission caused by the pump beam. The Pump and Probe beams are modulated at 500 kHz and 553 kHz respectively, and cross-polarized so the pump beam is filtered out before measurements.

5.1: Experimental Setup

The $MoSe_2$ heterostructure was mounted inside of a Montana X-Plane Cryostation cooled to 7 K. We use a 0.65 NA objective mounted inside of the Cryostation to image and measure the sample;

the beam is then transmitted through the sample and sapphire and collected into a lens that is focused into a photodiode as shown in Figure 5-1a. Figure 5-1b shows the heterostructure on a Sapphire substrate encapsulated by two ~10-15 nm thick hBN layers. The hBN thickness is chosen to mitigate surface roughness effects and screening environmental doping and fields.

The pump and probe beam are modulated at different frequencies (500 kHz and 553 kHz) and both are cross-polarized; in doing so, we treat the polarization of the beams as a parameter to filter, which then filters out the pump-designated beam. Only the probe is measured on the Photodiode as a result, which is then connected to a Lock-In Amplifier set at the difference frequency between the beam modulation frequencies (53 kHz). The result of this is a $\chi^{(3)}$ effect, discussed in detail in Chapter 4.4.

5.2: Results of Steady-Steady Pump-Probe Spectroscopy

Figure 5-2 shows the normalized PL spectrum of the sample, taken at 7 K and excited by a 20 μW green (532.8) diode laser, showing both the neutral and the charged exciton. This corresponds to a number density of ~10^8 cm^{-2}, indicating a relatively small amount of doping within this heterostructure[32]. Figure 5-2 also shows the normalized linear transmission signal showing a dip at the exciton resonance. The transmission signal was measured using a 20 μW continuous-wave (cw) laser scanned from 740 nm to 780 nm. Figure 5-3a shows a spectra obtained from the nonlinear spectroscopy measurement, using two cross-linearly polarized pump and probe beams set to a power of 100 μW and 20μW respectively. Using the pump and probe beams, we measure DT/T as a function of the pump and probe beam energy.

The spectrum shows unique features observed at 4 different combinations of pump and probe energies, which we call X/X (pumped at exciton energy and probed at exciton energy), X/T (pumped at exciton energy, probed at trion energy), T/X, and T/T referring to the energies of the pump and probe beams, respectively. In the cross-linearly polarized regime, we observe pump-induced redshifts at all three energies, with the strongest peak-to-peak signal observed at X/X. However, because the pump and probe are both cross-linearly polarized, this data results from mixed valley pseudo-spins, contrast to cross-circular polarization which excites one valley with the pump and the other with the probe.

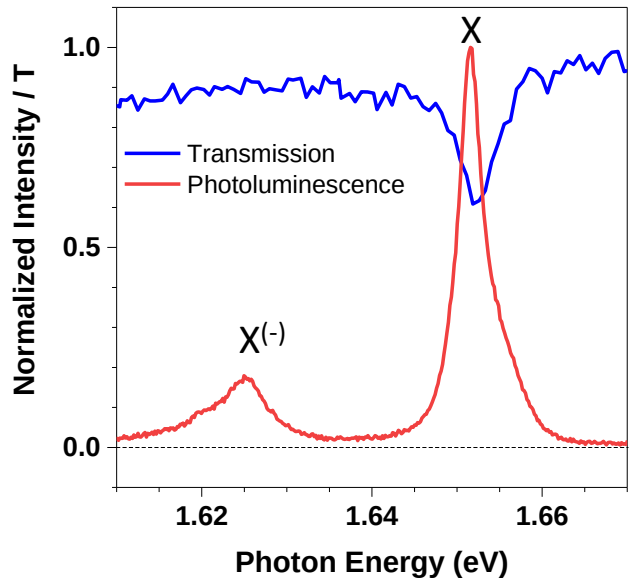

Figure 5-2. Normalized PL and linear transmission spectra measurement at 7 K, showing the neutral exciton and trion. The neutral exciton is located at 1.652 eV and the trion is located at 1.626 eV.

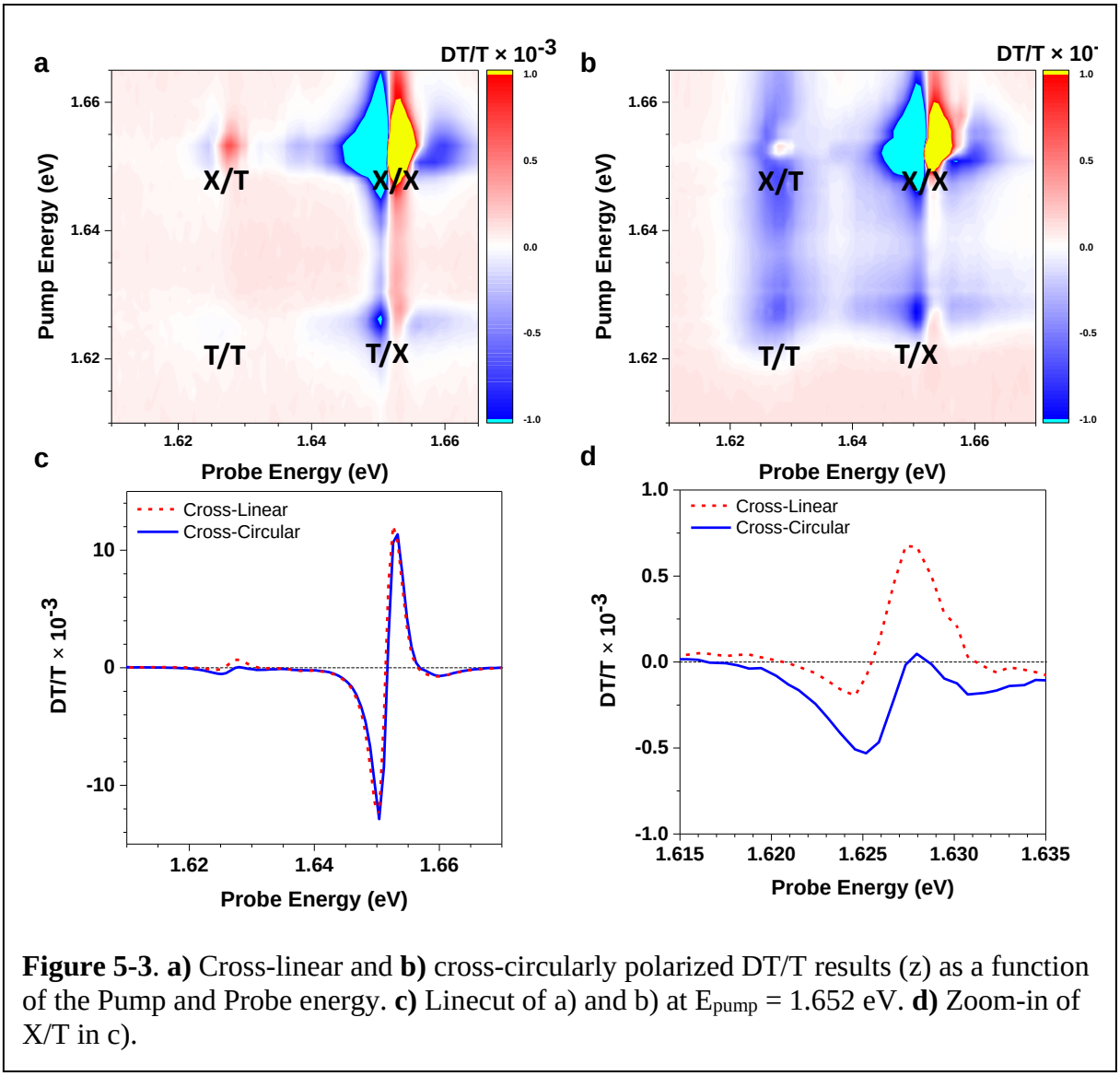

Figure 5-3. **a)** Cross-linear and **b)** cross-circularly polarized DT/T results (z) as a function of the Pump and Probe energy. **c)** Linecut of a) and b) at E_{pump} = 1.652 eV. **d)** Zoom-in of X/T in c).

Figure 5-3b shows the corresponding results using cross-circularly polarized pump and probe beams. While we observe a redshift at X/X and T/X as we did in the cross-linear regime, we also observe a "hole" feature which does not exist in the cross-linearly polarized regime. In pump energy we observe neighboring troughs to the "hole" feature. Figure 5-3d is a localized line cut at X/T, which indicates that the feature resembles the neighboring troughs but with an isolated peak at only X/T.

In Figure 5-4, we observe the power dependence of this signal held at E_{pump} = 1.652 and scanned over the probe energy. We observe that the peak effect only shows up at high power; at low power it resembles the pump-neighboring features at X/T. Previous measurements have shown that there are biexciton signals in TMDs which exist in the nonlinear regime[90].

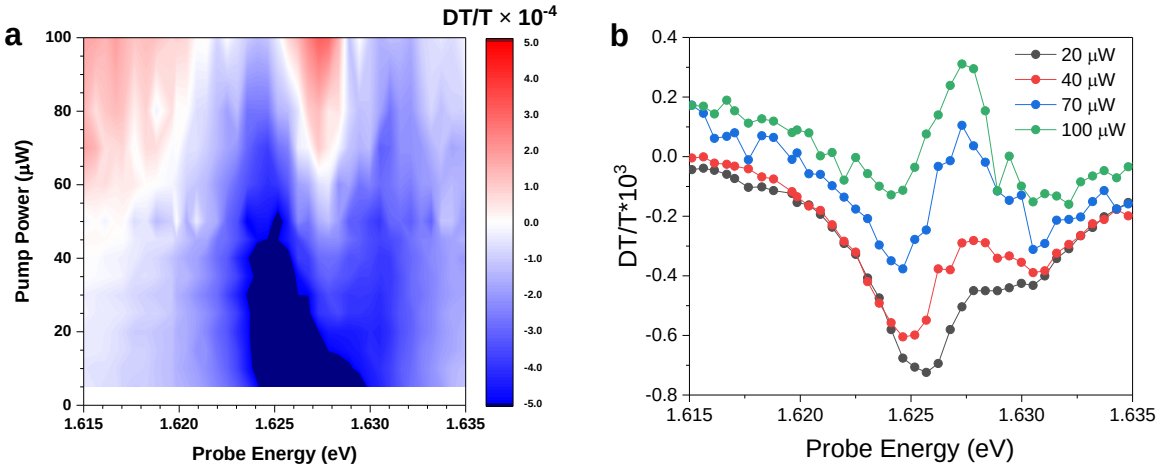

Figure 5-4. a) DT/T signal as a function of pump power (pump energy = 1.652 eV). **b**) Linecuts at certain pump powers from Figure 5-3b.

5.3: Applications of 3- and 4-Level Models to Experimental Result

In Chapter 3, I described the density matrix formalism as applied to 3- and 4-level models. Here, we investigate the possibility that our experimental results can be explained using a 3- or 4- level density matrix model. Our model considers three energy levels (Figure 2-1), with the first excited level referring to a single exciton state, and the second excited level referring to a biexciton state with a binding energy of 26 meV. The 4-level model (Figure 2-2) uses a degenerate single-exciton state to represent the K and -K valley, with the biexciton state above them. Therefore, signals originating from a pump or probe photon energy of 1.626 eV will refer to a biexciton signal (BX).

Each element of the density matrix refers to the corresponding transition within each state; for instance, ρ_{12} refers to the transition between the ground state and the exciton state. The optical response of the sample is directly proportional to the imaginary part of each element of the density matrix; therefore, we can adjust our model to take the difference between a field-off and field-on configuration.

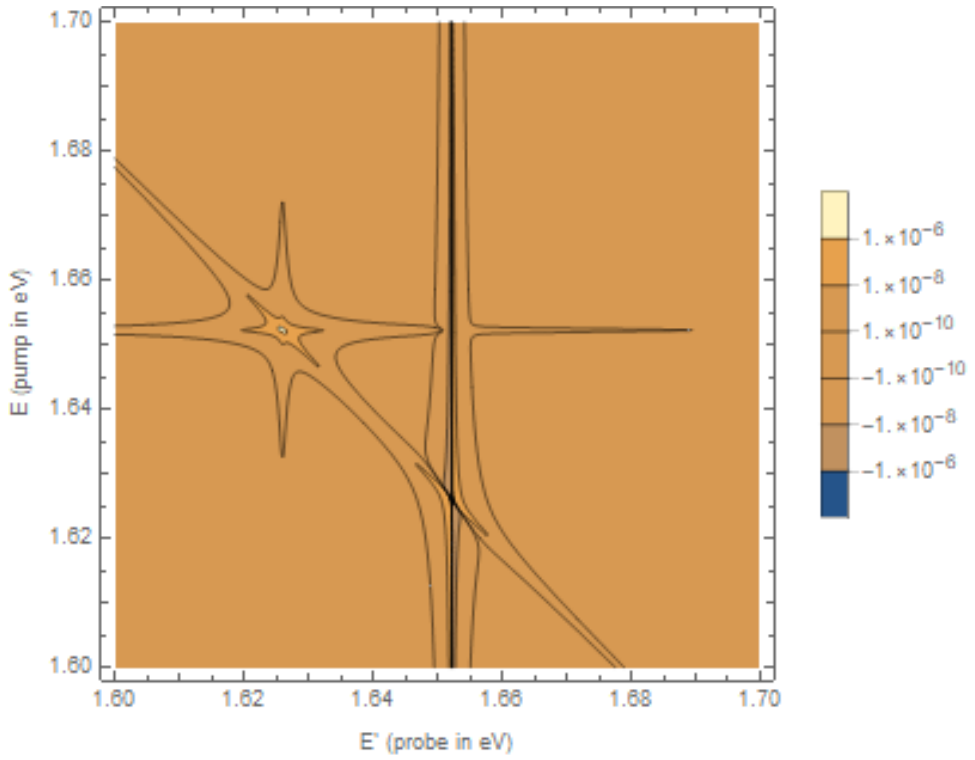

Figure 5-5. DT/T signal produced by the 3-level model according to Equation 5.01b. There are resonances observed at the exciton and biexciton resonances.

We modelled the exciton-biexciton system as a three-level ladder system using Figure 2-1. The top energy of the ladder is the trion energy, whereas the bottom energy level of the ladder is the negative of the exciton energy. To replicate the signal shape of the pump-probe experiment, we use Equation 5.01 to calculate DT/T.

$$\rho = \rho[Pump\ Power, Probe\ Power]\ (5.01a)$$

$$\frac{DT}{T} \sim Im\big[\rho_{12}[100\ \mu W, 20\ \mu W] - \rho_{12}[100\ \mu W, 0] + \rho_{23}[100\ \mu W, 20\ \mu W]$$

$$- \rho_{23}[100\ \mu W, 0]\big]\ (5.01b)$$

Figure 5.5 shows the results from the 3-level system as a function of pump and probe energies. The model shows resonances at the X/BX, BX/X, and X/X resonances as expected, with similar line-shapes at X/X and BX/X to our measurements. However, the 3-level model does not account for the valley pseudospin resulting from the cross-circularly polarized excitations. To account for this, we use the 4-level system from Figure 2-2, where both valleys are degenerate in energy. Using similar considerations to Equation 5.01b, 4-level signal can be generated with Equation 5.02;

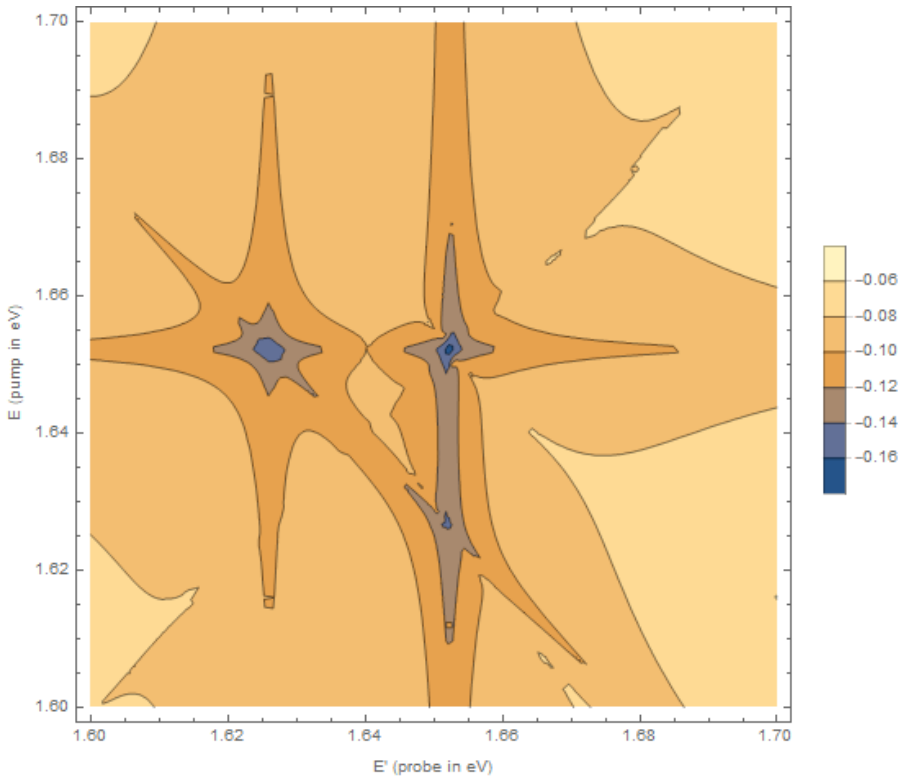

Figure 5-6. DT/T signal produced by the 4-level model in accordance to Equation 5.2b.

$$Signal = Im\big[\rho_{12}[100\ \mu W, 20\ \mu W] - \rho_{12}[100\ \mu W, 0] + \rho_{13}[100\ \mu W, 20\ \mu W] - \rho_{13}[100\ \mu W, 0] + \rho_{24}[100\ \mu W, 20\ \mu W] - \rho_{24}[100\ \mu W, 0] + \rho_{34}[100\ \mu W, 20\ \mu W] - \rho_{34}[100\ \mu W, 0]\big] \quad (5.02)$$

Figure 5-6 shows the results from the 4-level model. The model shows similar features to the 3-level model, but the magnitude of each signal is adjusted. The 4-level biexciton model shows agreement with the data at the resonance points, however there is missing oblique "line" feature between the X/BX and BX/X signals in our measurements. Due to the small relative magnitude of the oblique line feature, it is possible that this is a feature that we lack the sensitivity to detect. Another explanation is that the oblique line comes from our definition that $E_{pump} + E_{probe} = \pm(\omega_1 + \omega_2)$. While we can replicate the general lineshapes of our experiment, we cannot replicate the intensity of the signal and resulting mathematical artifacts reduce the accuracy of the multi-level system as a model when examined away from resonance. We therefore cannot conclude that this is a biexciton signature resulting from an exciton pump and trion probe, and therefore we require a more robust theory to explain these effects.

5.4: T-Matrix Formalism Applied to Semiconductor TMDs

We used a theoretical model to analyze the data using a T-matrix approach[57], used for the third order nonlinear response of semiconductor quantum wells[58]. The T-matrix approach describes 2-particle scattering in terms of linear susceptibilities, in this case the particles are excitons and trions. We can use a 2-particle scattering framework to work with $MoSe_2$, with the particles in this model being an exciton and a trion. The T-matrix model depicted in Figure 3. The results of the T-matrix model are shown in Figure 5-7, which shows great agreement with the data obtained in

Figure 5-3. We will discuss the parameter tuning of the T-matrix approach in-depth in this section and compare them to the resonant linecuts of Figure 5-7. Note that pump and probe resonances of 1.626 eV will refer to the trion (T) in this formalism.

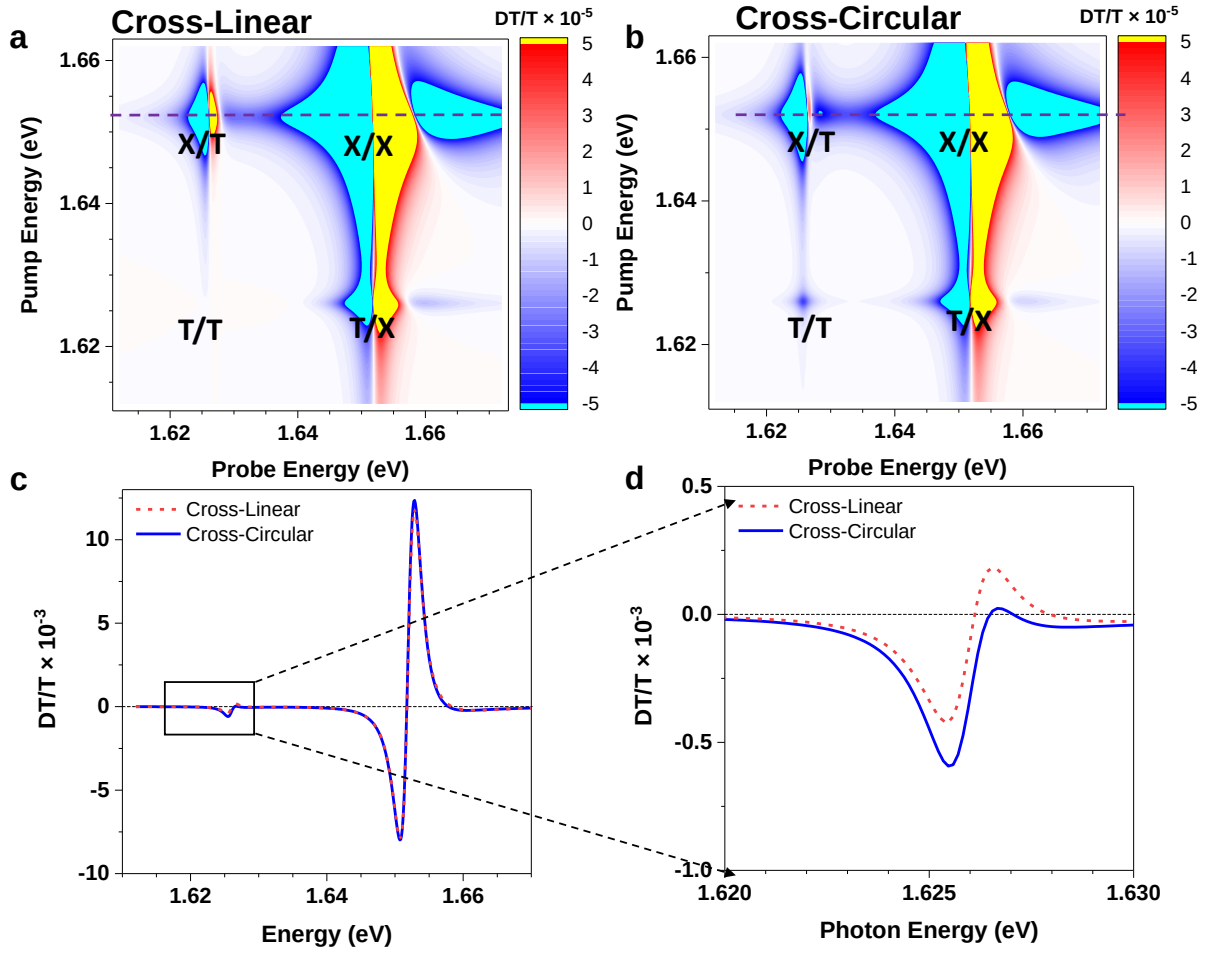

Figure 5-7. Theoretical calculation of DT/T spectra from Figure 5-3 with **a)** cross-linearly excitation and **b)** cross-circular excitation, showing strong agreement in all configurations. **c)** DT/T linecuts when pumped at the exciton resonance in cross-linear and cross-circular configurations. **d)** Close-up of the trion section of the DT/T spectrum.

5.4.1: Exciton Lineshapes

We start our discussion by looking at the exciton (~1.652 eV) signal in the cross-circular channel. In the cross-circular channel, the pump and probe beams create excitons in opposite valleys leading to intervalley interactions. Figure 5-8 depicts our model without the electron-hole (e-h) interaction exchange, showing the previously observed signatures of the biexciton[53,54] manifesting as a dip around 10 meV below the neutral exciton. The biexciton signal is positive-negative here, consistent with previous observations with GaAs[91]. The experimental data shows that there is a redshift (negative-positive) at the exciton resonance rather than a blueshift (positive-negative), which is a direct result of the e-h exchange interaction. The e-h exchange interaction destabilizes the biexciton in our system, meaning that there is no bound biexciton state in the system. However, in both

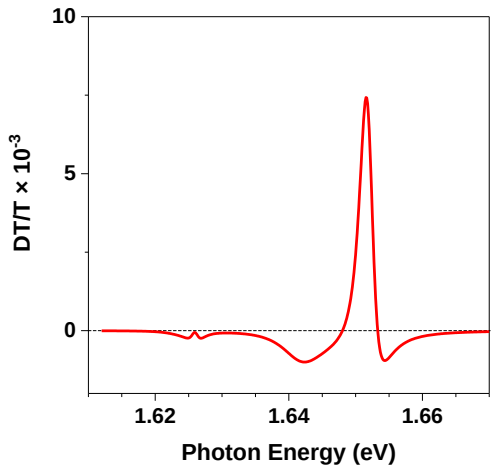

Figure 5-8. Theoretical DT/T in the cross-circular configuration without the e-h exchange.

Figures 5-3 and 5-7, there is a negative DT/T signal when pumped at exciton and probed above the exciton resonance, which is attributed to being a trace of the biexciton.

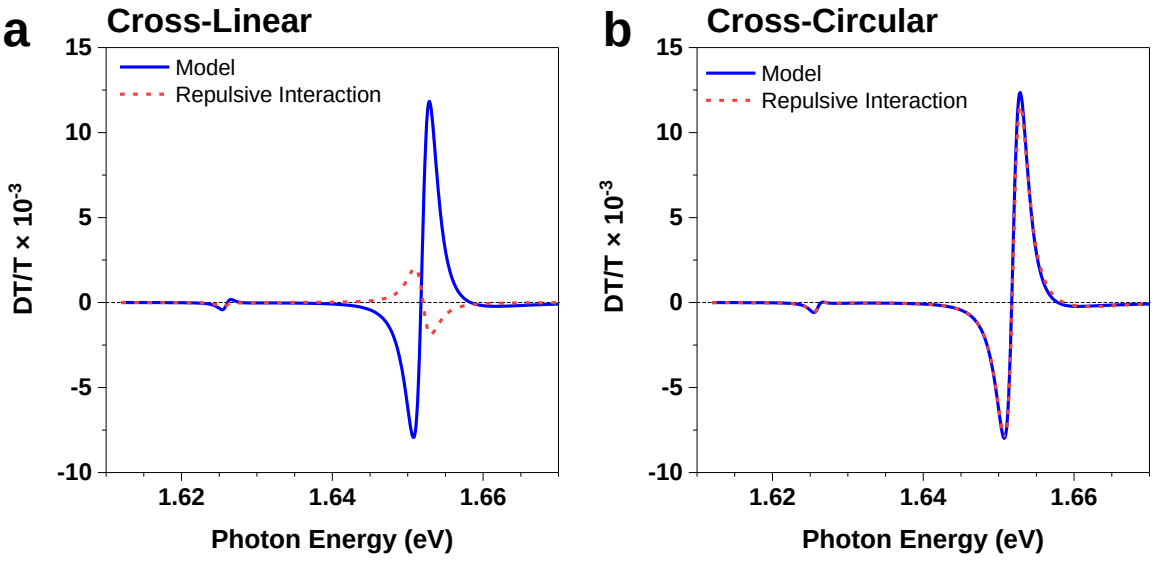

Figure 5-9. Theoretical DT/T spectra of our model vs the model with the repulsive interaction, which would be appropriate in the coherent nonlinear optical regime) included. **a)** Using the repulsive or attractive interaction has negligible effect on the DT/T in the cross-circular configuration. **b)** In the cross-linear configuration, the model with the repulsive interaction included shows a blue-shift signal at the exciton, which is a significant divergence from the experimental signal, therefore justifying our use of an attractive interaction in our model.

We now analyze the cross-linear channel. In the cross-linear channel, both pump and probe create excitons in both valleys, leading to stronger intravalley effects such as spin-mixing and exciton repulsion. Previously we have observed blueshifts in the co-circular and the cross-linear channels in the coherent regime, noting that there is a relationship $DT_{co\text{-}circular} = 2\ DT_{cross\text{-}linear}$[58]. These two channels have similar mechanisms to create a blue-shift, resulting from the strong exciton-exciton repulsion effects from either populating one valley strongly (co-circular) or populating both valleys simultaneously (cross-linear). As a result of this large population, we expect to see a

blueshift. However, the experimental results indicate a redshift in the signal, which means that the redshift is a result of spin-mixing which would not occur in the co-circular channel. As a result, we choose the sign of the interaction in the cross-linearly polarized response to be negative (representing an attractive interaction).

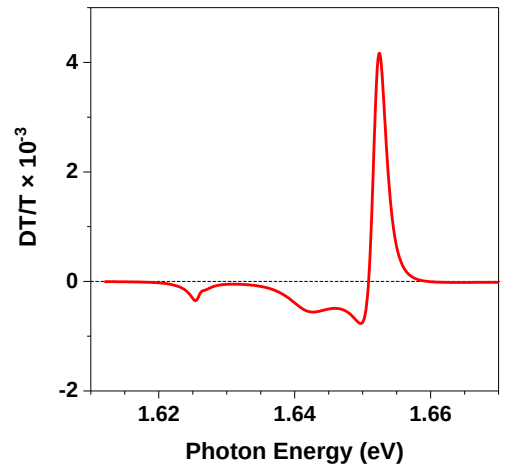

Figure 5-10. Theoretical DT for cross-circular configuration, but in contrast to our standard parameters, here the intervalley e-h exchange is not reduced.

We can see in Figure 5-9 that this choice in sign for the interaction causes negligible impact on the cross-circular channel, as expected. However, despite this the signal is still dominated by the blueshift, resulting directly from the e-h intervalley exchange. Therefore, to justify our reduction in the intervalley exchange, Figure 5-10 shows our model with full intervalley e-h exchange factored in. In this iteration of the model, the signal lacks a distinct negative feature at the exciton.

5.4.2: Trion Lineshapes

We now discuss the lineshapes at the trion resonances (~1.626 eV). The lineshapes when probed at trion are much closer to the linear trion resonance which dominates the DT signal. This DT signal appears to match with a simple resonance enhancement, where more trion states can be filled due the effects of the pump beam. We can therefore conclude that the lineshape is dictated by the exciton-trion complex. However, the trion signal in the cross-circular channel has a notably more negative signal than the trion signal in the cross-linear channel. The theory can reproduce

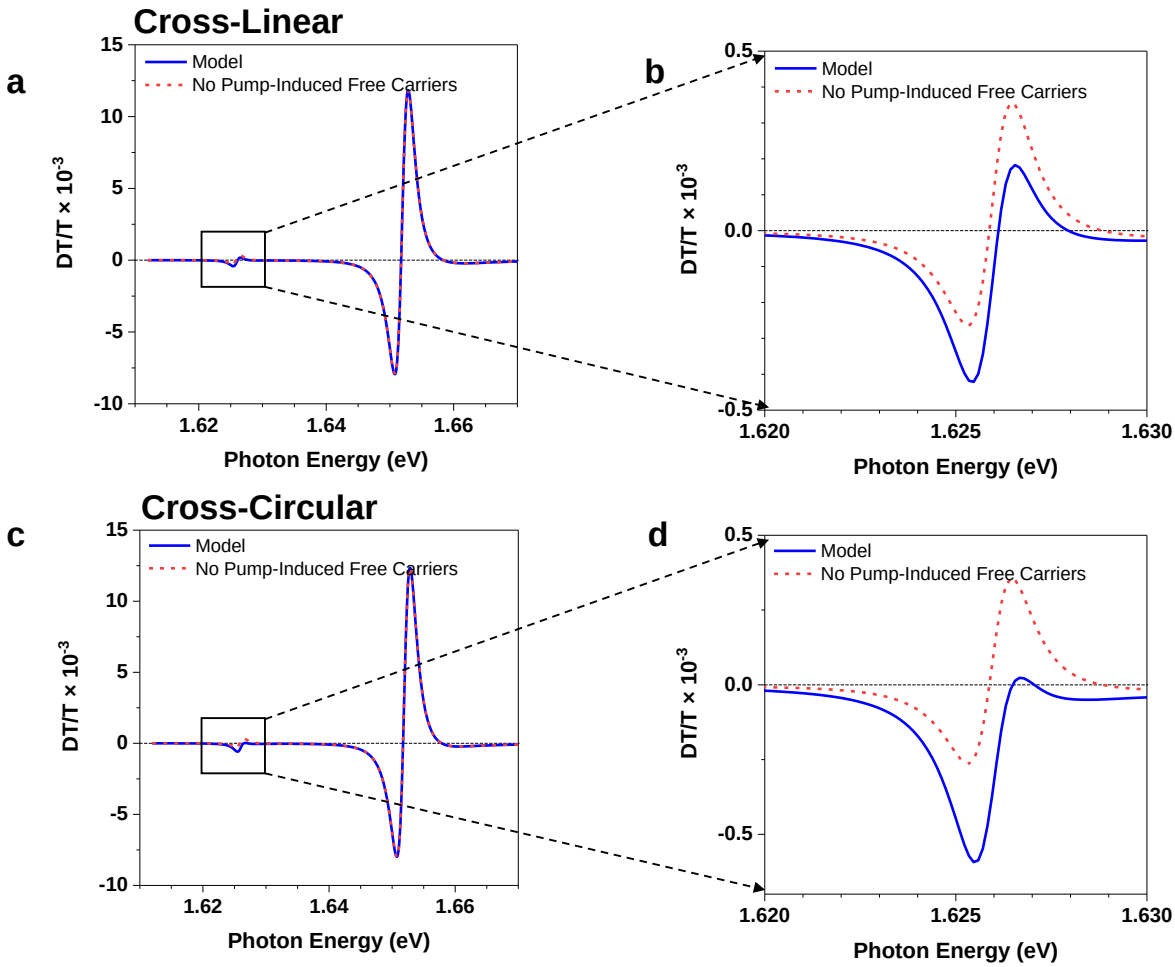

Figure 5-11. Comparison of our model parameters without pump induced free carriers (blue) and with (red). The signal at the exciton shows good agreement with the experiment in both cases, whereas the signal at the trion agrees better with the experiment when the effect of the pump-induced free carriers is taken into account. **a)** and **b)** cross-linear configuration, **c)** and **d)** show the cross-circular configuration.

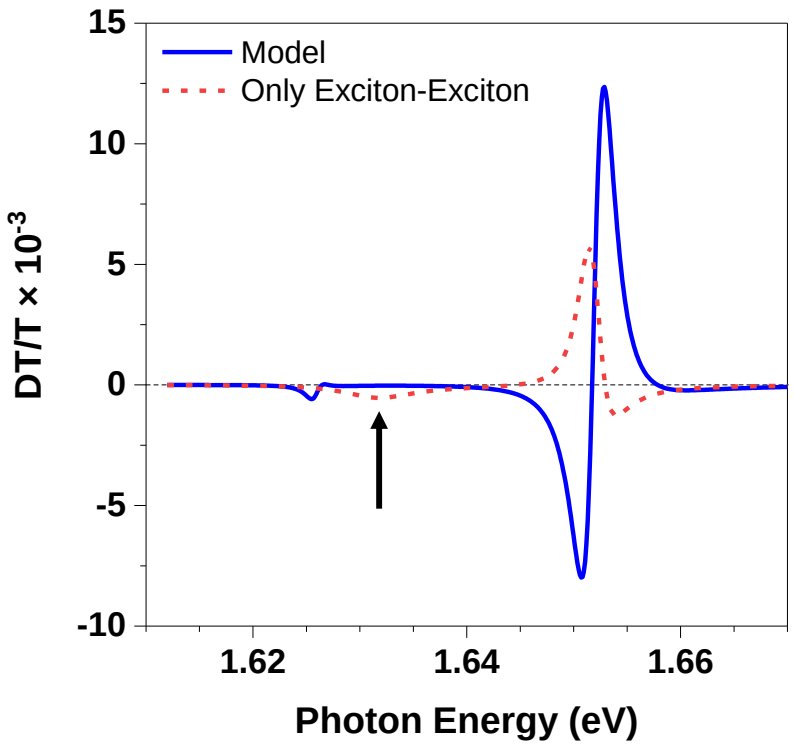

Figure 5-12. Comparison of our theoretical model (solid blue) to a model which does not include: trions (including no exciton-trion and trion-interaction) or e-h exchange. In other words, a model with only a strong exciton-exciton interaction (dashed red) in the cross-circular configuration. This shows a small biexciton peak at 1.632 eV, meaning that the data does not support the formation of a bound biexciton.

this feature when accounting for pump-induced free carrier generation. Using the estimate that our pump-induced free carrier density is on the order of 10^8 cm^{-2} (from the trion photoluminescence signal) as shown in Figure 5-11. we believe this is sufficiently low enough density that we can produce free carriers through our pump beam. In other words, the DT signal produced when probed at the trion is a result of a linear trion resonance mixed with the exciton-trion complex. In Figure 5-12, we switch off the exciton-trion and trion-trion interactions and increase the exciton-exciton interaction to $u_0^2 = 8eV\text{Å}^2$; this results in a weak biexciton peak of 1.632 eV, further emphasizing a lack of bound biexciton signature in our signal.

5.4.3: Calculation Parameters

In Figure 5-7 we presented the theoretical DT spectrum obtained from the T-matrix formalism obtained with the following parameters. Note that throughout this section, we use the notation of Kwong et. al[57].

Parameter	Value
Electron mass (m_e)	$0.83m_0$
Exciton mass (m_x)	$2m_e$
Trion mass (m_t)	$3m_e$
Exciton-exciton interaction strength (u_0^2)	6 eVÅ^2
Exciton-trion interaction strength	$0.6u_0^2$
Trion-trion interaction strength	$0.2u_0^2$
Trion oscillator strength ($\|f_i\|^2 n'_{ei}$)	$0.02\|\mu_i\|^2$
Trion excitation amplitude ($\|f_i\|^2$)	$4\,\pi\, a_{tr}^2$ (trion Bohr radius[92])
Trion binding energy	26 eV
Free-electron density	$0.87 \times 10^{11}\text{cm}^{-2}$
Pump-induced free-carrier density	$3.3 \times 10^{8}\text{cm}^{-2}$
Intravalley e-h exchange (η_{intra})	1
Intervalley e-h exchange (η_{inter})	$0.2\eta_{intra}$
Exciton (trion) dephasing	2 meV (1 meV)

Table 5-1. Parameters used with the T-matrix formalism.

Conclusion

We have applied our method of measuring the steady state non-linear response to an hBN-encapsulated $MoSe_2$ device and examined two theories to explain the observed lineshapes at resonance. While the density matrix formalism, under the assumption of a bound exciton-trion biexciton, replicates general features of our data, it fails to explain some of the negative features above the X/X point as well as the purely negative linear susceptibility signal at trion resonances. It also fails to explain the power dependent "hole" signal which appears solely at the cross-circular X/T point. In response we developed a T-matrix formalism, originally adapted to GaAs, with application to TMD semiconductors to replicate each feature. We see that the theory incorporates exciton-trion correlations, spin-mixing and relaxation, electron-hole interaction, the absence of a bound biexciton resulting in strong exciton-exciton interactions which create our lineshapes.

Chapter 6 - Conclusion and Future Directions

In this thesis, we examined the properties of van der Waals heterostructures based on $MoSe_2$, a TMD heterostructure with tightly bound excitons. We discussed examples of heterostructures we can construct using materials such as graphene and hBN to finely tune and probe various properties of the material such as the number density. In Chapter 2 we introduced methods to fabricate layered van der Waals heterostructures and connect them to an electrical source. The process of fabrication included exfoliation of bulk crystals, searching through the substrates, characterization, stacking, and lithography on both conductive and insulating substrates. In Chapter 3 we discuss the fundamentals of non-linear optics, as well as form a density matrix formalism for a multi-level system to discuss measured non-linear signals. I also introduced the T-matrix formalism which combines the interplay of different exciton states to form various transmission based signals. In Chapter 4 we discussed our non-linear measurement setup, consisting of two continuous wave lasers modulated at different frequencies to allow us to track the pump-induced change to the probe signal using a lock-in amplifier.

In Chapter 5 we demonstrated the use of our non-linear optical technique to perform continuous wave steady-state pump-probe spectroscopy at 7 K on an hBN-encapsulated $MoSe_2$. We observe redshifts in the transmission signal when the signal is pumped and probed at resonance, and we observe a linear trion resonance when the signal is probed at resonance. We observe these redshifts for both cross-circularly and cross-linearly polarized light, both as a result of their electron-hole interactions. However the cross-circularly polarized light also has spin-mixing and relaxation effects at play due to filling up both valleys.

We also observe small positive features at both the cross-circularly and cross-linearly polarized portion of the X/T regime of our plot, which are a mix of signals between the linear trion resonance and a pump-induced free carrier density.

6.1: Future Directions

The recent implementation of the T-matrix to describe the non-linear transmission response of $MoSe_2$ has opened the door to similar steady-state non-linear measurements of various other TMD semiconductors. We can also stack TMD monolayers together into moiré heterostructures[59,93–95], such as $MoSe_2/WSe_2$ and use steady state non-linear spectroscopy to probe any relaxation effects arising from the interaction between the interlayer exciton and the exciton resonances of each individual TMD. Previous measurements have been performed showing the interactions occurring within interlayer excitons[96], but a systematic study has not yet been performed.

We have also realized a method to create precise EBL patterns on insulating substrates (such as sapphire), which opens the door to measurements which we can finely tune the carrier density such that a charged exciton species dominates. This allows us to probe the interactions between a trion and exciton states as a function of charge density which has yet to be explored.

References

1. Geim, A. K. & Grigorieva, I. V. Van der Waals heterostructures. *Nature* **499**, 419–425 (2013).
2. Novoselov, K. S. *et al.* A roadmap for graphene. *Nature* **490**, 192–200 (2012).
3. Banerjee, S., Richardson, W., Coleman, J. & Chatterjee, A. A new three-terminal tunnel device. *IEEE Electron Device Lett.* **8**, 347–349 (1987).
4. Tributsch, H. The $MoSe_2$ Electrochemical Solar Cell: Anodic Coupling of Electron Transfer to d → d Photo-Transitions in Layer Crystals. *Berichte Bunsenges. Für Phys. Chem.* **82**, 169–174 (1978).
5. Coehoorn, R. *et al.* Electronic structure of $MoSe_2$, MoS_2 , and WSe_2 . I. Band-structure calculations and photoelectron spectroscopy. *Phys. Rev. B* **35**, 6195–6202 (1987).
6. Butler, S. Z. *et al.* Progress, Challenges, and Opportunities in Two-Dimensional Materials Beyond Graphene. *ACS Nano* **7**, 2898–2926 (2013).
7. Rokni, H. & Lu, W. Direct measurements of interfacial adhesion in 2D materials and van der Waals heterostructures in ambient air. *Nat. Commun.* **11**, 5607 (2020).
8. Liu, Y. *et al.* Van der Waals heterostructures and devices. *Nat. Rev. Mater.* **1**, 1–17 (2016).
9. Wang, H. *et al.* Two-dimensional heterostructures: fabrication, characterization, and application. *Nanoscale* **6**, 12250–12272 (2014).
10. Craciun, M. F. *et al.* Trilayer graphene is a semimetal with a gate-tunable band overlap. *Nat. Nanotechnol.* **4**, 383–388 (2009).
11. Gamayun, O. V., Gorbar, E. V. & Gusynin, V. P. Gap generation and semimetal-insulator phase transition in graphene. *Phys. Rev. B* **81**, 075429 (2010).
12. Jiang, T. *et al.* Gate-tunable third-order nonlinear optical response of massless Dirac fermions in graphene. *Nat. Photonics* **12**, 430–436 (2018).

13. Hendry, E., Hale, P. J., Moger, J., Savchenko, A. K. & Mikhailov, S. A. Coherent Nonlinear Optical Response of Graphene. *Phys. Rev. Lett.* **105**, 097401 (2010).
14. Cheng, J. L., Vermeulen, N. & Sipe, J. E. Third-order nonlinearity of graphene: Effects of phenomenological relaxation and finite temperature. *Phys. Rev. B* **91**, 235320 (2015).
15. Furchi, M. *et al.* Microcavity-Integrated Graphene Photodetector. *Nano Lett.* **12**, 2773–2777 (2012).
16. Nair, R. R. *et al.* Fine Structure Constant Defines Visual Transparency of Graphene. *Science* **320**, 1308–1308 (2008).
17. Zhan, D. *et al.* Engineering the Electronic Structure of Graphene. *Adv. Mater.* **24**, 4055–4069 (2012).
18. Gui, G., Li, J. & Zhong, J. Band structure engineering of graphene by strain: First-principles calculations. *Phys. Rev. B* **78**, 075435 (2008).
19. Bolotin, K. I. *et al.* Ultrahigh electron mobility in suspended graphene. *Solid State Commun.* **146**, 351–355 (2008).
20. Novoselov, K. S. *et al.* Two-dimensional gas of massless Dirac fermions in graphene. *Nature* **438**, 197–200 (2005).
21. Park, C.-H., Yang, L., Son, Y.-W., Cohen, M. L. & Louie, S. G. Anisotropic behaviours of massless Dirac fermions in graphene under periodic potentials. *Nat. Phys.* **4**, 213–217 (2008).
22. Yu, W. J. *et al.* Highly efficient gate-tunable photocurrent generation in vertical heterostructures of layered materials. *Nat. Nanotechnol.* **8**, 952–958 (2013).
23. Cheng, R. *et al.* Multifunctional tunneling devices based on graphene/*h*-BN/$MoSe_2$ van der Waals heterostructures. *Appl. Phys. Lett.* **110**, 173507 (2017).

24. Xue, J. *et al.* Scanning tunnelling microscopy and spectroscopy of ultra-flat graphene on hexagonal boron nitride. *Nat. Mater.* **10**, 282–285 (2011).
25. Zomer, P. J., Guimarães, M. H. D., Brant, J. C., Tombros, N. & van Wees, B. J. Fast pick up technique for high quality heterostructures of bilayer graphene and hexagonal boron nitride. *Appl. Phys. Lett.* **105**, 013101 (2014).
26. Watanabe, K., Taniguchi, T. & Kanda, H. Direct-bandgap properties and evidence for ultraviolet lasing of hexagonal boron nitride single crystal. *Nat. Mater.* **3**, 404–409 (2004).
27. Cassabois, G., Valvin, P. & Gil, B. Hexagonal boron nitride is an indirect bandgap semiconductor. *Nat. Photonics* **10**, 262–266 (2016).
28. Britnell, L. *et al.* Electron Tunneling through Ultrathin Boron Nitride Crystalline Barriers. *Nano Lett.* **12**, 1707–1710 (2012).
29. Le, C. T. *et al.* Nonlinear optical characteristics of monolayer $MoSe_2$: Nonlinear optical characteristics of monolayer $MoSe_2$. *Ann. Phys.* **528**, 551–559 (2016).
30. Liu, G. *et al.* Third-order nonlinear optical properties of $MoSe_2$/graphene composite materials. *Opt. Laser Technol.* **120**, 105746 (2019).
31. Arora, A., Nogajewski, K., Molas, M., Koperski, M. & Potemski, M. Exciton band structure in layered $MoSe_2$: from a monolayer to the bulk limit. *Nanoscale* **7**, 20769–20775 (2015).
32. Ross, J. S. *et al.* Electrical control of neutral and charged excitons in a monolayer semiconductor. *Nat. Commun.* **4**, 1474 (2013).
33. Wang, G. *et al.* Exciton states in monolayer $MoSe_2$: impact on interband transitions. *2D Mater.* **2**, 045005 (2015).
34. Mo, S.-K. *et al.* Spin-resolved photoemission study of epitaxially grown $MoSe_2$ and WSe_2 thin films. *J. Phys. Condens. Matter* **28**, 454001 (2016).

35. Mak, K. F., He, K., Shan, J. & Heinz, T. F. Control of valley polarization in monolayer MoS_2 by optical helicity. *Nat. Nanotechnol.* **7**, 494–498 (2012).
36. Xiao, D., Liu, G.-B., Feng, W., Xu, X. & Yao, W. Coupled Spin and Valley Physics in Monolayers of MoS_2 and Other Group-VI Dichalcogenides. *Phys. Rev. Lett.* **108**, 196802 (2012).
37. Kane, B. E. A silicon-based nuclear spin quantum computer. *Nature* **393**, 133–137 (1998).
38. Wolf, S. A. Spintronics: A Spin-Based Electronics Vision for the Future. *Science* **294**, 1488–1495 (2001).
39. Lee, C. *et al.* Comparison of trapped charges and hysteresis behavior in hBN encapsulated single MoS_2 flake based field effect transistors on SiO_2 and hBN substrates. *Nanotechnology* **29**, 335202 (2018).
40. Thomsen, J. D. *et al.* Suppression of intrinsic roughness in encapsulated graphene. *Phys. Rev. B* **96**, 014101 (2017).
41. Courtade, E. *et al.* Spectrally narrow exciton luminescence from monolayer MoS_2 and $MoSe_2$ exfoliated onto epitaxially grown hexagonal BN. *Appl. Phys. Lett.* **113**, 032106 (2018).
42. Bao, D. Optical study of excitonic complexes in transition metal dichalcogenides monolayers. (Nanyang Technological University, 2020).
43. Li, L. H., Cervenka, J., Watanabe, K., Taniguchi, T. & Chen, Y. Strong Oxidation Resistance of Atomically Thin Boron Nitride Nanosheets. *ACS Nano* **8**, 1457–1462 (2014).
44. Holler, J. *et al.* Air tightness of hBN encapsulation and its impact on Raman spectroscopy of van der Waals materials. *2D Mater.* **7**, 015012 (2019).

45. Murthy, A. A. *et al.* Intrinsic Transport in 2D Heterostructures Mediated through h-BN Tunneling Contacts. *Nano Lett.* **18**, 2990–2998 (2018).

46. Laturia, A., Van de Put, M. L. & Vandenberghe, W. G. Dielectric properties of hexagonal boron nitride and transition metal dichalcogenides: from monolayer to bulk. *Npj 2D Mater. Appl.* **2**, 6 (2018).

47. Wang, Q. H., Kalantar-Zadeh, K., Kis, A., Coleman, J. N. & Strano, M. S. Electronics and optoelectronics of two-dimensional transition metal dichalcogenides. *Nat. Nanotechnol.* **7**, 699–712 (2012).

48. Sun, Z., Martinez, A. & Wang, F. Optical modulators with 2D layered materials. *Nat. Photonics* **10**, 227–238 (2016).

49. Lee, E., Yoon, Y. S. & Kim, D.-J. Two-Dimensional Transition Metal Dichalcogenides and Metal Oxide Hybrids for Gas Sensing. *ACS Sens.* **3**, 2045–2060 (2018).

50. Singh, A. *et al.* Coherent Electronic Coupling in Atomically Thin $MoSe_2$. *Phys. Rev. Lett.* **112**, 216804 (2014).

51. Martin, E. W. *et al.* Encapsulation Narrows and Preserves the Excitonic Homogeneous Linewidth of Exfoliated Monolayer $MoSe_2$. *Phys. Rev. Appl.* **14**, 021002 (2020).

52. Hao, K. *et al.* Coherent and Incoherent Coupling Dynamics between Neutral and Charged Excitons in Monolayer $MoSe_2$. *Nano Lett.* **16**, 5109–5113 (2016).

53. Hao, K. *et al.* Neutral and charged inter-valley biexcitons in monolayer $MoSe_2$. *Nat. Commun.* **8**, 15552 (2017).

54. Yong, C.-K. *et al.* Biexcitonic optical Stark effects in monolayer molybdenum diselenide. *Nat. Phys.* **14**, 1092–1096 (2018).

55. Yong, C.-K. *et al.* Valley-dependent exciton fine structure and Autler–Townes doublets from Berry phases in monolayer $MoSe_2$. *Nat. Mater.* **18**, 1065–1070 (2019).

56. Waterman, P. C. Matrix formulation of electromagnetic scattering. *Proc. IEEE* **53**, 805–812 (1965).

57. Kwong, N.-H., Schaibley, J. R. & Binder, R. Effect of intravalley and intervalley electron-hole exchange on the nonlinear optical response of monolayer $MoSe_2$. *ArXiv. 210800091 Cond-Mat Physics* (2021).

58. Takayama, R., Kwong, N.-H., Rumyantsev, I., Kuwata-Gonokami, M. & Binder, R. Material and light-pulse parameter dependence of the nonlinear optical susceptibilities in the coherent $\chi^{(3)}$ regime in semiconductor quantum wells. *JOSA B* **21**, 2164–2174 (2004).

59. Takayama, R., Kwong, N., Rumyantsev, I., Kuwata-Gonokami, M. & Binder, R. T-matrix analysis of biexcitonic correlations in the nonlinear optical response of semiconductor quantum wells. *Phys. Condens. Matter* **25**, 445–462 (2002).

60. Novoselov, K. S. Electric Field Effect in Atomically Thin Carbon Films. *Science* **306**, 666–669 (2004).

61. Yankowitz, M. *et al.* Emergence of superlattice Dirac points in graphene on hexagonal boron nitride. *Nat. Phys.* **8**, 382–386 (2012).

62. Kumar, N. *et al.* Second harmonic microscopy of monolayer MoS_2. *Phys. Rev. B* **87**, 161403 (2013).

63. Lucking, M. C., Beach, K. & Terrones, H. Large second harmonic generation in alloyed TMDs and boron nitride nanostructures. *Sci. Rep.* **8**, 10118 (2018).

64. Wen, X., Gong, Z. & Li, D. Nonlinear optics of two-dimensional transition metal dichalcogenides. *InfoMat* **1**, 317–337 (2019).

65. Xia, J., Yan, J. & Shen, Z. X. Transition metal dichalcogenides: structural, optical and electronic property tuning via thickness and stacking. *FlatChem* **4**, 1–19 (2017).
66. Malard, L. M., Pimenta, M. A., Dresselhaus, G. & Dresselhaus, M. S. Raman spectroscopy in graphene. *Phys. Rep.* **473**, 51–87 (2009).
67. Tang, B., Guoxin, H. & Gao, H. Raman Spectroscopic Characterization of Graphene. *Appl. Spectrosc. Rev.* **45**, 369–407 (2010).
68. Giessibl, F. J. Advances in atomic force microscopy. *Rev. Mod. Phys.* **75**, 949–983 (2003).
69. Rosenberger, M. R. *et al.* Nano-"Squeegee" for the Creation of Clean 2D Material Interfaces. *ACS Appl. Mater. Interfaces* **10**, 10379–10387 (2018).
70. Haigh, S. J. *et al.* Cross-sectional imaging of individual layers and buried interfaces of graphene-based heterostructures and superlattices. *Nat. Mater.* **11**, 764–767 (2012).
71. Stern, E. *et al.* Methods for fabricating Ohmic contacts to nanowires and nanotubes. *J. Vac. Sci. Technol. B Microelectron. Nanometer Struct.* **24**, 231 (2006).
72. Klein, M. *et al.* 2D semiconductor nonlinear plasmonic modulators. *Nat. Commun.* **10**, 3264 (2019).
73. Dibos, A. M. *et al.* Electrically Tunable Exciton–Plasmon Coupling in a WSe_2 Monolayer Embedded in a Plasmonic Crystal Cavity. *Nano Lett.* **19**, 3543–3547 (2019).
74. Kleemann, M.-E. *et al.* Strong-coupling of WSe_2 in ultra-compact plasmonic nanocavities at room temperature. *Nat. Commun.* **8**, 1296 (2017).
75. Kim, K. S. *et al.* Atomic layer etching of graphene through controlled ion beam for graphene-based electronics. *Sci. Rep.* **7**, 2462 (2017).

76. Prado, M. C., Jariwala, D., Marks, T. J. & Hersam, M. C. Optimization of graphene dry etching conditions via combined microscopic and spectroscopic analysis. *Appl. Phys. Lett.* **102**, 193111 (2013).
77. Ye, J., Yan, T., Niu, B., Li, Y. & Zhang, X. Nonlinear dynamics of trions under strong optical excitation in monolayer $MoSe_2$. *Sci. Rep.* **8**, 2389 (2018).
78. Rodek, A. *et al.* Local field effects in ultrafast light–matter interaction measured by pump-probe spectroscopy of monolayer $MoSe_2$. *Nanophotonics* **0**, 20210194 (2021).
79. Yao, P., He, D., Zereshki, P., Wang, Y. & Zhao, H. Nonlinear optical effect of interlayer charge transfer in a van der Waals heterostructure. *Appl. Phys. Lett.* **115**, 263103 (2019).
80. Schaibley, J. R. *et al.* Directional interlayer spin-valley transfer in two-dimensional heterostructures. *Nat. Commun.* **7**, 13747 (2016).
81. Valencia-Acuna, P. *et al.* Transient absorption of transition metal dichalcogenide monolayers studied by a photodope-pump-probe technique. *Phys. Rev. B* **102**, 035414 (2020).
82. Introduction to Acousto-Optic Modulators and Deflectors. *Gooch & Housego* (2015).
83. Mys, O., Kostyrko, M., Smyk, M., Krupych, O. & Vlokh, R. Anisotropy of acoustooptic figure of merit for TeO_2 crystals. 1. Isotropic diffraction. *Ukr. J. Phys. Opt.* **15**, 132 (2014).
84. Feng, Y., Vinogradov, I. & Ge, N.-H. General noise suppression scheme with reference detection in heterodyne nonlinear spectroscopy. *Opt. Express* **25**, 26262 (2017).
85. Adaptive noise canceling for transient absorption microscopy. *J. Biomed. Opt.* **25**, (2020).
86. Pike, N. A. & Pachter, R. Second-Order Nonlinear Optical Properties of Monolayer Transition-Metal Dichalcogenides by Computational Analysis. *J. Phys. Chem. C* **125**, 11075–11084 (2021).

87. Torres-Torres, C. *et al.* Third order nonlinear optical response exhibited by mono- and few-layers of WS_2. *2D Mater.* **3**, 021005 (2016).

88. Woodward, R. I. *et al.* Characterization of the second- and third-order nonlinear optical susceptibilities of monolayer MoS_2 using multiphoton microscopy. *2D Mater.* **4**, 011006 (2016).

89. Walsh, A., Da Silva, J. L. F. & Wei, S.-H. Origins of band-gap renormalization in degenerately doped semiconductors. *Phys. Rev. B* **78**, 075211 (2008).

90. Pei, J. *et al.* Excited State Biexcitons in Atomically Thin $MoSe_2$. *ACS Nano* **11**, 7468–7475 (2017).

91. Sieh, C. *et al.* Coulomb Memory Signatures in the Excitonic Optical Stark Effect. *Phys. Rev. Lett.* **82**, 3112–3115 (1999).

92. Glazov, M. M. Optical properties of charged excitons in two-dimensional semiconductors. *J. Chem. Phys.* **153**, 034703 (2020).

93. Tran, K. *et al.* Evidence for moiré excitons in van der Waals heterostructures. *Nature* **567**, 71–75 (2019).

94. Liu, Y. *et al.* Moiré superlattices and related moiré excitons in twisted van der Waals heterostructures. *Chem. Soc. Rev.* **50**, 6401–6422 (2021).

95. Brem, S., Linderälv, C., Erhart, P. & Malic, E. Tunable Phases of Moiré Excitons in van der Waals Heterostructures. *Nano Lett.* **20**, 8534–8540 (2020).

96. Jin, C. *et al.* Identification of spin, valley and moiré quasi-angular momentum of interlayer excitons. *Nat. Phys.* **15**, 1140–1144 (2019).